The Astrophysical Journal, 805:58 (19pp), 2015 May 20 doi:10.1088/0004-637X/805/1/58

THE RELATIONSHIP BETWEEN THE DUST AND GAS-PHASE CO ACROSS THE CALIFORNIA MOLECULAR CLOUD

S. Kong[1], C. J. Lada[2], E. A. Lada[1], C. Román-Zúñiga[3], J. H. Bieging[4], M. Lombardi[5], J. Forbrich[6], and J. F. Alves[6]
[1] Astronomy Department, University of Florida, Gainesville, FL 32611, USA; skong@astro.ufl.edu
[2] Harvard-Smithsonian Center for Astrophysics, 60 Garden Street, Cambridge, MA 02138, USA
[3] Instituto de Astronomía, Universidad Nacional Autónoma de México, Unidad Académica en Ensenada, Km 103 Carr. Tijuana-Ensenada, 22860 Ensenada BC, Mexico
[4] Steward Observatory, The University of Arizona, Tucson, AZ 85719, USA
[5] Department of Physics, University of Milan, Italy
[6] University of Vienna, Vienna, Austria
Received 2014 September 26; accepted 2015 March 10; published 2015 May 20

ABSTRACT

We present results of an extinction-CO line survey of the southeastern part of the California molecular cloud (CMC). Deep, wide-field, near-infrared images were used to construct a sensitive, relatively high resolution (~0.5 arcmin) (NICEST) extinction map of the region. The same region was also surveyed in the ^{12}CO(2–1), ^{13}CO(2–1), and C^{18}O(2–1) emission lines at the same angular resolution. These data were used to investigate the relation between the molecular gas, traced by CO emission lines, and the dust column density, traced by extinction, on spatial scales of 0.04 pc across the cloud. We found strong spatial variations in the abundances of ^{13}CO and C^{18}O that were correlated with variations in gas temperature, consistent with temperature-dependent CO depletion/desorption on dust grains. The ^{13}CO-to-C^{18}O abundance ratio was found to increase with decreasing extinction, suggesting selective photodissociation of C^{18}O by the ambient UV radiation field. The effect is particularly pronounced in the vicinity of an embedded cluster where the UV radiation appears to have penetrated deeply (i.e., $A_V \lesssim 15$ mag) into the cloud. We derived the cloud-averaged *X*-factor to be $\langle X_{CO} \rangle = 2.53 \times 10^{20}$ cm^{-2}(K km s^{-1})$^{-1}$, a value somewhat higher than the Milky Way average. On sub-parsec scales we find there is no single empirical value of the ^{12}CO *X*-factor that can characterize the molecular gas in cold ($T_k \lesssim 15$ K) cloud regions, with $X_{CO} \propto A_V^{0.74}$ for $A_V \gtrsim 3$ mag. However, in regions containing relatively hot ($T_{ex} \gtrsim 25$ K) molecular gas we find a clear correlation between $W(^{12}CO)$ and A_V over a large ($3 \lesssim A_V \lesssim 25$ mag) range of extinction. This results in a constant $X_{CO} = 1.5 \times 10^{20}$ cm^{-2} (K km s^{-1})$^{-1}$ for the hot gas, a lower value than either the average for the CMC or the Milky Way. Overall we find an (inverse) correlation between X_{CO} and T_{ex} in the cloud with $X_{CO} \propto T_{ex}^{-0.7}$. This correlation suggests that the global *X*-factor of a giant molecular cloud may depend on the relative amounts of hot gas contained within the cloud.

Key words: dust, extinction – ISM: abundances – ISM: clouds – stars: formation

1. INTRODUCTION

The relationship between the dust and gas in a molecular cloud is crucial in understanding the cloud properties and the star formation activities therein. Dust provides the most reliable and useful tracer of the total gas column density (e.g., Bohlin et al. 1978; Goodman et al. 2009), while molecules like ^{13}CO and C^{18}O are more useful as tracers of the local physical and chemical conditions (e.g., gas temperatures and velocities, CO column densities, etc). A comparison between them allows us to probe the variation of molecular gas abundances, i.e., [^{13}CO] and [C^{18}O] ([molecule] $\equiv N$(molecule)/N(H), where N is column density), caused by such factors as photodissociation and chemical depletion/desorption in cold/warm environments. This helps to reveal the physical and chemical properties of the molecular cloud, which enables us to better understand the initial conditions of star formation and its potential dependence on such factors as cloud chemistry and structure. Such variations have been noted in previous observations of a variety of giant molecular clouds (GMCs), including Perseus (Pineda et al. 2008), Taurus (Pineda et al. 2010), and Orion (Ripple et al. 2013), made at relatively high spatial resolutions (0.2–0.4 pc). Here we report the results of a combined CO-dust extinction study of the California molecular cloud (CMC; Lada et al. 2009) at even higher spatial resolution (~0.04 pc) in order to investigate in more detail the relation between CO gas and dust in this interesting nearby GMC.

The CMC is a useful laboratory for such studies. In particular, it contains a massive filamentary structure in its southeast region that consists of both cold molecular gas with little star formation activity and hot molecular gas associated with an active star-forming region containing the massive star LkHα 101 and its accompanying embedded cluster. This provides a physical environment with large temperature and density variations that are interesting to explore. Indeed, as reported in Lada et al. (2009), the CMC overall shows an order-of-magnitude lower star formation rate (SFR) than the Orion molecular cloud, even though these equally distant GMCs have similar mass, size, and morphology. Recently, Li et al. (2014) also found the ^{13}CO clumps in the CMC to be characterized by similar kinematic states as those in Orion. Lada et al. (2009) proposed that the difference in SFRs between the two clouds was a result of a difference in cloud structure, specifically the amount of dense gas in each cloud. Moreover, this close connection between dense gas mass and the SFR appears to be a general physical property of galactic GMCs (Lada et al. 2010). It would be of interest to compare

other properties of the CMC with similar ones in the Orion cloud to look for additional factors, such as cloud chemistry, for example, that could contribute to the difference in the SFR between the two clouds.

A combined CO-extinction study can also be used to investigate the CO *X*-factor ($X_{\rm CO} \equiv N({\rm H_2})/W_{\rm CO(1-0)}$, where W is integrated intensity), which is widely used to derive molecular cloud masses from the CO(1–0) line flux, especially in external galaxies (see, e.g., Bolatto et al. 2013; Sandstrom et al. 2013). Despite being very optically thick, this CO rotational transition is still thought to be a good tracer for the total molecular gas mass, due to the effect of photon transport in gas with large velocity gradients. However, variations of physical conditions can have an effect on the *X*-factor and, in many instances, render its application rather uncertain. Apparently, there is no universally valid *X*-factor (see recent review from Bolatto et al. 2013). Consequently, investigating the dependence of the *X*-factor on differing physical conditions is clearly of great interest in establishing practical guidelines for its application. Combined CO-extinction studies of nearby clouds can therefore provide potentially important insights into this issue.

In this paper, we present observational results of molecular lines ^{12}CO(2–1), ^{13}CO(2–1), and C^{18}O(2–1). The total gas mass (or $N_{\rm H_2}$) is traced by extinction derived from near-infrared observations, independent from the molecular lines. The area covered in our observations is mainly dense gas with $A_{\rm V} \gtrsim 3$ mag. With the NICEST technique (Lombardi 2009), we are able to trace extinction up to $A_{\rm V} \sim 33$ mag, which is much deeper than achieved in a similar study of Orion by Ripple et al. (2013), who used the NICER technique (Lombardi & Alves 2001) to trace extinction depths up to $A_{\rm V} \sim 15$ mag. We also observed the optically thinner C^{18}O (2–1) line, which provides insights into CO chemistry (e.g., Lada et al. 1994; Shimajiri et al. 2014) that cannot be readily derived using only ^{12}CO and ^{13}CO observations.

In the following, we describe our observations and data reduction in Section 2. We present the results and analysis in Section 3. Discussions and conclusions will be presented in Section 4 and Section 5, respectively.

2. OBSERVATIONS AND DATA REDUCTION

2.1. Near-infrared Wide-field Mapping Survey

2.1.1. Telescope and Observations

Near-IR (NIR) observations for this study were obtained at the 3.5 m telescope of the Centro Astronómico Hispano Alemán observatory (hereafter CAHA) at Calar Alto in Almería, Spain. Our observations were made with the OMEGA 2000 camera, which has a field of view of 15′. In this paper we report observations for eight fields that cover the L1482 region. These fields are part of a more comprehensive survey of the CMC with a total of 24 fields. Fields CN01 to CN08 (Table 1) were observed in the three main NIR broad bands, *J*, *H*, and K_s, between 2009 October and 2010 January, with acceptable weather and seeing, except for one field, CN03, which was repeated on 2012 December. All observations consisted of 20 exposures of 60 s, co-added as 1200 s exposure mosaics. The fields observed with the CAHA 3.5 m telescope were selected to cover the main filament or "spine" of L1482, including the region of the LkHα 101 cluster. The pixel scale of OMEGA 2000 at the 3.5 m telescope is 0.45 arcsec pixel^{-1}, with excellent uniformity and negligible geometric distortion across the FOV.

A list of all fields observed and considered for final analysis can be consulted in Table 1. The table lists the field identification, the center of field positions, observation date, filter, an estimate of the seeing based on the average FWHM of the stars detected in each field, and the peak values for the brightness distributions, which are a good measurement of the sensitivity limits achieved. Below, we describe the observations and the data reduction process, including the construction of the photometric catalogs used to make our dust extinction map.

2.1.2. Near-infrared Data Reduction and Calibration

The NIR image data from OMEGA 2000 were reduced with pipelines that made use of standard IRAF procedures complemented with stand-alone routines. These pipelines are based on the FLAMINGOS NIR reduction, photometry, and astrometry pipelines (Levine 2006; Román-Zúñiga 2006). The data process is essentially identical to the one described in Román-Zúñiga et al. (2010), and we refer the reader to that paper for details.

Both photometry and astrometry of OMEGA 2000 data products were calibrated relative to Two Micron All Sky Survey (2MASS) lists obtained from the All-Sky Point Source Catalog (PSC). The final photometry catalogs were merged with a combination of TOPCAT-STIL (Taylor 2005) and IDL routines. In the case of adjacent fields, overlapping areas were treated with a routine designed to handle duplicate detections in such a way that we list preferentially a higher-quality observation (e.g., a smaller photometric uncertainty) over a lower-quality one.

The 2MASS data were also used to replace observations for saturated stars in all our frames. We used, in all cases, lists retrieved from the 2MASS All-Sky PSC at the IPAC. The final photometry catalogs, containing either *J, H*, and K_s or *H* and K_s photometry, were merged with a combination of TOPCAT-STIL (Taylor 2005) and self-made IDL routines.

2.2. The CO Molecular-line Survey

2.2.1. Telescope and Observations

A series of observations were carried out with the Heinrich Hertz Sub-millimeter Telescope (SMT) on Mount Graham, Arizona, from 2011 November to 2012 April. The SMT is located at an elevation of 3200 meters. The receiver has prototype ALMA Band 6 sideband separating mixers with two orthogonal polarizations. Typical single sideband system temperatures during the observing were around 200 K. The molecular lines ^{12}CO(2–1) (230.538 GHz), ^{13}CO(2–1) (220.399 GHz), and C^{18}O(2–1) (219.560 GHz) were observed over a selection of 17 10′ × 10′ square regions (hereafter "tiles") along the southeastern dense ridge of the CMC, roughly at R.A. = $04^{\rm h}30^{\rm m}00^{\rm s}$, decl. = 35°50′00″ (see Figure 1; also Figure 1 of Lada et al. 2009). These tiles have $A_{\rm V} \gtrsim 3$ mag and cover the higher-extinction regions of the cloud, as well as the LkHα 101 cluster (roughly centered in tile 12).

In each tile, we performed the observations using the "on-the-fly (OTF)" mode. The scanning rate was 10″ per second along the direction of right ascension (R.A.), with each row being separated by 10″ in declination (decl.). Each sampling point has a 0.4 s integration, corresponding to 4″ spatial

Table 1
Near-infrared Observations of L1482 Fields

Field ID	Date Obs.	Center Coords. J2000		Filter	Seeing (″)	LF Peak[a] (mag)
CALAR ALTO 3.5 m OMEGA 2000 OBSERVATIONS						
CN-01	2009 Dec 24	04:30:58.81	+34:51:57.5	J	1.49	19.00
CN-01	2009 Dec 24	04:30:58.81	+34:51:57.5	H	1.52	19.75
CN-01	2009 Dec 24	04:30:58.81	+34:51:57.5	K_s	1.39	19.25
CN-02	2009 Dec 08	04:30:38.55	+35:04:20.4	J	1.36	19.50
CN-02	2009 Oct 09	04:30:38.55	+35:04:20.4	H	1.59	20.75
CN-02	2009 Oct 09	04:30:38.55	+35:04:20.4	K_s	1.47	19.75
CN-03	2012 Dec 23	04:30:07.84	+35:16:06.6	J	1.11	22.25
CN-03	2012 Dec 23	04:30:07.84	+35:16:06.6	H	1.06	20.25
CN-03	2012 Dec 23	04:30:07.84	+35:16:06.6	K_s	1.12	19.25
CN-04	2009 Oct 07	04:30:44.04	+35:27:49.5	J	1.05	21.25
CN-04	2009 Oct 07	04:30:44.04	+35:27:49.5	H	0.96	19.50
CN-04	2009 Oct 09	04:30:44.04	+35:27:49.5	K_s	1.05	21.50
CN-05	2009 Oct 07	04:30:44.04	+35:41:24.1	J	0.91	21.25
CN-05	2009 Oct 07	04:30:44.04	+35:41:24.1	H	0.93	22.00
CN-05	2009 Oct 06	04:30:44.04	+35:41:24.1	K_s	1.17	19.75
CN-06	2009 Oct 06	04:30:44.73	+35:54:54.8	J	1.29	22.00
CN-06	2009 Oct 06	04:30:44.73	+35:54:54.8	H	1.26	21.00
CN-06	2009 Oct 06	04:30:44.73	+35:54:54.8	K_s	1.30	20.00
CN-07	2010 Jan 02	04:29:08.58	+36:29:18.7	J	1.07	20.75
CN-07	2010 Jan 02	04:29:08.58	+36:29:18.7	H	1.13	19.00
CN-07	2010 Jan 02	04:29:08.58	+36:29:18.7	K_s	1.18	18.75
CN-08	2010 Jan 03	04:28:16.37	+36:29:58.4	J	1.37	20.25
CN-08	2010 Jan 03	04:28:16.37	+36:29:58.4	H	1.35	20.00
CN-08	2010 Jan 03	04:28:16.37	+36:29:58.4	K_s	1.02	19.25

Note.
[a] Expresses turnover point of observed magnitude distribution.

Table 2
CO Survey Tile Properties

Tile	$\overline{T}_{ex}$ (K)	Slope[a] (10^{16} cm^{-2} mag^{-1})	r-value[a]
01	9.21	0.014	0.42
02	9.31	0.027	0.65
03	8.30	0.031	0.64
04	8.52	0.025	0.50
05	9.14	0.024	0.57
06	9.23	0.018	0.43
07	9.99	0.046	0.64
08	9.19	0.037	0.55
09	12.3	0.034	0.37
10	12.3	0.066	0.67
11	13.1	0.148	0.80
12	19.6	0.193	0.76
13	16.5	0.204	0.91
14	16.9	0.102	0.62
15	9.07	0.059	0.75
16	8.65	0.054	0.64
17	9.66	0.022	0.64

Note.
[a] Linear regression results from Figure 6. In tiles 11–14, the fitting is performed over the entire A_V range. In the rest of the tiles, the fitting is up to $A_V = 10$ mag. The r-value (Pearson coefficient) is an estimation of correlation coefficient.

sampling in R.A. with a beam size around 35″; therefore, the source is fully sampled. The total integration time for each tile is roughly 1 hr. We utilized dual-sideband mode and had two distinct sets of observations: Obs1: ^{13}CO(2–1) in lower sideband (LSB) and ^{12}CO(2–1) in upper sideband (USB); Obs2: C^{18}O(2–1) in LSB and ^{12}CO(2–1) in USB. In each set, two orthogonal linear polarizations were observed simultaneously. The total bandwidth we cover with the spectrometer is 128 channels of 0.25 MHz each or 32 MHz total, for each line (^{12}CO, ^{13}CO, and C^{18}O). The channel resolution is 0.25 MHz, set by the filter widths, and this corresponds to about 0.34 km s^{-1} velocity resolution, depending on the line rest frequencies via the Doppler formula. We checked the pointing on the compact nearby CO source CRL 618 (R.A. = 04^{h}43^{m}42^s.9, decl. = 36°08′14″.7) at the beginning of every tile. The 5 s integrations were performed on each point of a five-point cross pattern centered on that source. The pointing error was typically $\lesssim$5″. To calibrate the intensity, we observed the strong CO source W3OH (R.A. = 02^{h}27^{m}59^s.2, decl. = 61°55′43″.2) between every two tiles.

2.2.2. Millimeter-wave Data Reduction

All data were first processed through the CLASS software package. We fitted linear baselines and subtracted them from the data. The data image cubes were ported into MIRIAD software format (Sault et al. 1995) for further analysis and display. OTF data were interpolated onto regular grids with grid spacing of 10″ before being stored into the MIRIAD data set. Next, the data were calibrated using W3OH. A scale factor is derived through the observation toward W3OH between every two tiles. The factor is used to scale the antenna temperature T_A^* to the main-beam brightness temperature T_{mb} (see Bieging et al. 2010 for details). For each molecular

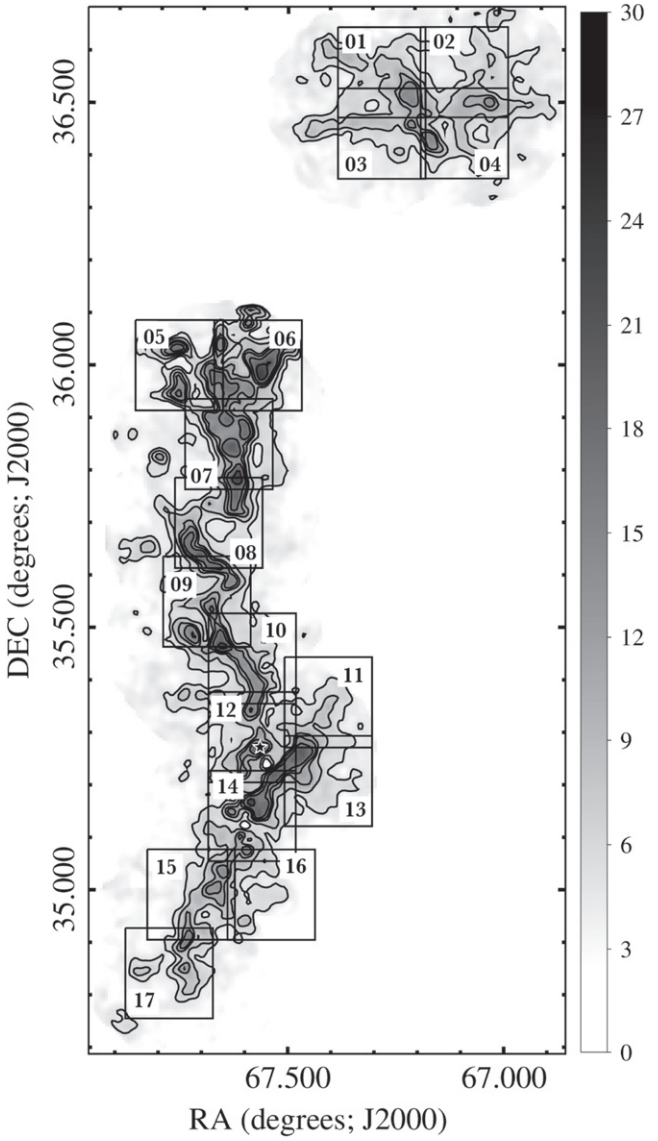

Figure 1. Contour map of visual extinction derived from our near-infrared survey with the NICEST method. Contours at intervals of A_V = (5, 7, 10, 12, 15, 20, 25, and 30 mag). See descriptions in Section 2.1. The square boxes outline the 17 tiles representing the areas surveyed in CO emission. LkHα 101 is marked by the star in tile 12.

transition, the two polarizations were averaged to increase the signal-to-noise ratio (S/N). Finally, all 17 tiles were combined together to form a single map (weighted by their rms noise at the small overlapped area). The original data cube, with ~0.34 km s^{-1} velocity channels (set by the 0.25 MHz filter bandwidth), was re-sampled onto a 0.15 km s^{-1} spacing, by third-order polynomial interpolation. This re-sampling puts all of the CO isotopologues on exactly the same velocity grid, so we can make ratio maps, for example. We convolved all maps with Gaussian kernels (FWHM = 18.″1 for ^{12}CO map, FWHM = 13.″6 for ^{13}CO and C^{18}O maps) to have a final map resolution (FWHM) of 38″ with a grid spacing of 19″ in order to match the resolution of and facilitate direct comparison with our dust extinction maps.

We calculated the rms noise for all emission-free channels in each map to be about 0.1 K for all three lines. We compared the integrated intensity maps of the two sets of ^{12}CO maps by subtracting one from the other. We found a small spatial difference (typically $\lesssim$10″ between each pair of corresponding tiles), and we shifted and re-gridded Obs1 ^{12}CO and ^{13}CO maps to Obs2. We averaged the two sets of ^{12}CO maps weighted by their rms noise to lower the noise in the averaged ^{12}CO map to 0.07 K (rms).

3. RESULTS AND ANALYSIS

3.1. The NICEST Dust Extinction Map

Figure 1 shows the deep dust extinction map of the southeast portion of the CMC derived from our observations. For this map Calar Alto data were supplemented with data from 2MASS in some outer portions of the surveyed area where Calar Alto data were not available. Also shown are the boundaries of the 17 tiles of the multi-line CO mapping survey. The extinction map was constructed with the optimized version of the Near Infrared Color Excess Revised (NICER) technique, known as NICEST (Lombardi & Alves 2001; Lombardi 2009). The NICER/NICEST technique allows us to measure dust extinction from the infrared excess in the colors of background stars caused by dust absorption. The excess is derived by assuming as intrinsic colors the colors of stars detected in a nearby off-cloud control field with negligible extinction (see Table 1). For the measurements of extinction, we avoid the use of sources with intrinsic color excess, such as candidate young stellar objects and dusty galaxies. NICEST is essentially identical to NICER, except that the A_V estimator is modified to account for small-scale inhomogeneities, due to a bias introduced by the decrease in the number of observable stars as extinction increases toward the denser areas of a molecular cloud. The bias is removed by modifying the estimator with an additional term that accounts for the expected decrement.

Extinction measurements for individual sources are smoothed with a Gaussian filter with an FWHM of 38″, and the maps are constructed with 19″ spatial sampling. At each (line-of-sight) position in the map, each star falling within the beam is given a weight calculated from a Gaussian function and the inverse of the variance squared, which is in turn also used for the bias-correction factor. A preliminary value of A_V at the map position is calculated as the weighted median of all possible values within the beam. Then, we estimate the mean absolute deviation (m.a.d.) of these values to remove large deviates using m.a.d.-clipping. The remaining values are used by the NICEST estimator to calculate the final A_V at the corresponding position.

In the case of pixel positions where only 2MASS sources are available, the number of sources per beam is significantly smaller, and there are cases where there are not enough stars to estimate A_V; in those cases, our code increases the size of the beam by a factor of 2 over the nominal value. The nominal 38″ FWHM of our maps represents an increase of resolution by a factor of 2.1 compared to the earlier study of Lada et al. (2009). This resolution is comparable to the beam size of the CO maps. The resulting noise of the extinction map is 0.05 mag for $A_V <$ 10 mag and 0.1 mag for $A_V \geqslant$ 10 mag.

3.2. CO Spectra and Integrated Intensity Maps

In order to provide an overview of the observations and the general quality of the data, we first show in Figure 2 the averaged CO spectra derived for each of the 10′ × 10′ tiles of our mapping grid. On this coarse scale (1.3 × 1.3 pc) the ^{12}CO

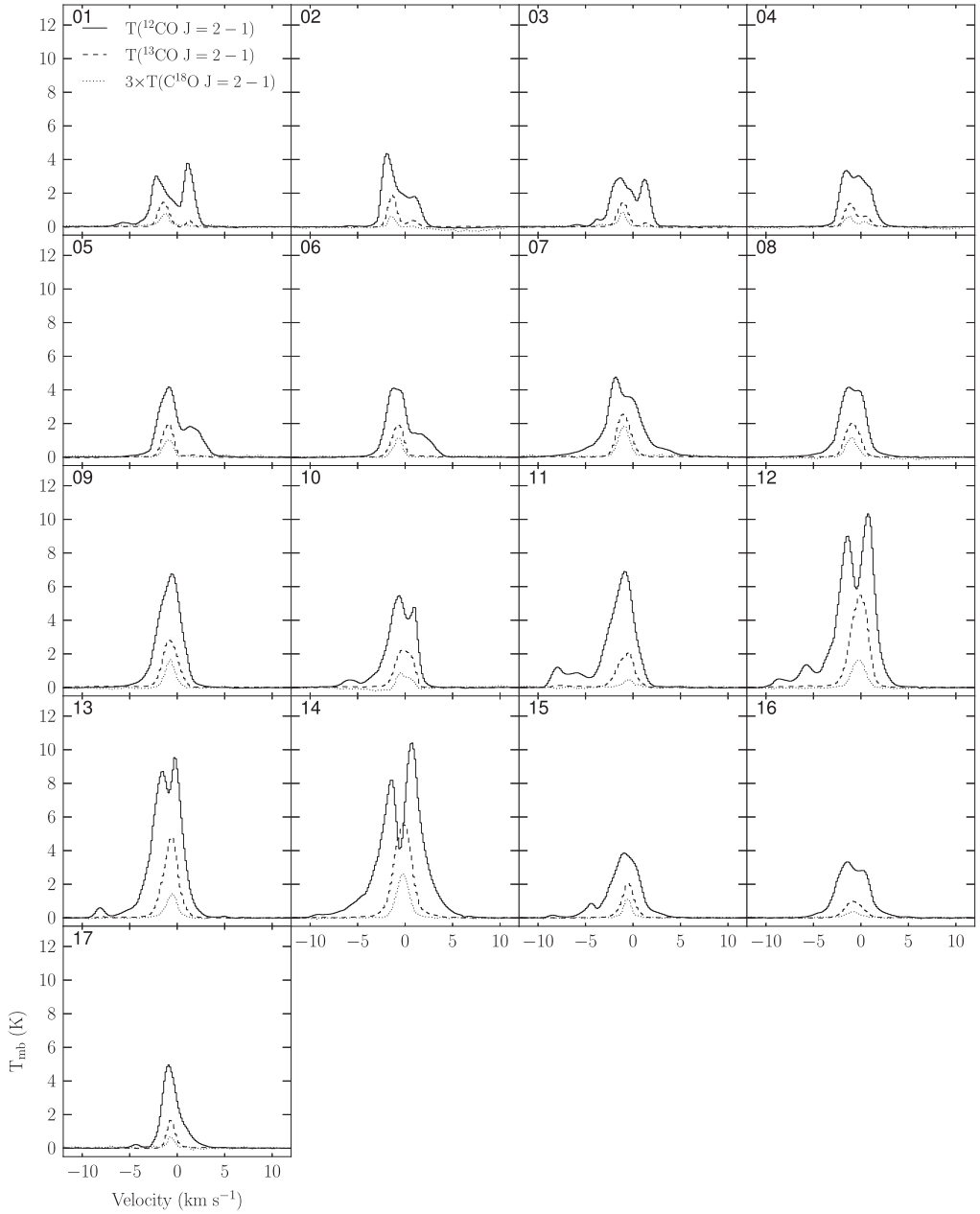

Figure 2. Averaged spectra for all three molecular lines in each $10' \times 10'$ tile. Roughly 1000 spectra (from 1000 pixels) in each tile were averaged together. $C^{18}O(2–1)$ spectra were enlarged by a factor of 3 to be shown together with the other two line spectra.

profiles exhibit evidence for both self-absorption and multi-component structure. The presence of self-absorption indicates that the ^{12}CO emission is quite optically thick. The profiles of the rarer isotopes appear to be less complex, mostly characterized by simple Gaussian-like shapes. Maps of the emission from $^{12}CO(2–1)$, $^{13}CO(2–1)$, and $C^{18}O(2–1)$ integrated over velocity ranges −12 to +10 km s^{-1}, −10 to +6 km s^{-1}, and −4 to +3 km s^{-1}, respectively, are shown in Figure 3 as grayscale maps with contours overlaid for clarity. The maps display some common morphological features. The strongest emission occurs in the mid-southern area (tiles 11–14, $\delta \approx 35^{\circ}.25$) and is in close proximity to the LkHα 101 cluster (which lies within tiles 10–12, $\delta \approx 35^{\circ}.27$). On close inspection of the maps, a sharp drop-off in CO emission is observed along a warm filamentary structure southwest of the cluster. This sharp drop in CO emission, together with the enhanced CO emission within the warm filament, likely indicates a physical interaction between the cluster stars and the filamentary ridge structure. A similar structure with an accompanying drop-off is also present in the extinction map of Figure 1. Here we can see that the warm filamentary structure is a small section of the more extended high-extinction ridge that forms the backbone of the cloud in this region and which is the subject of this survey. In these more extended regions away from the cluster, the CO emission is comparatively quiescent.

The rms noise for the integrated intensity maps σ_W (in K km s^{-1}) was first estimated using

$$\sigma_W = \sigma_c \times \frac{\Delta V}{\sqrt{N_{\rm channel}}}, \quad (1)$$

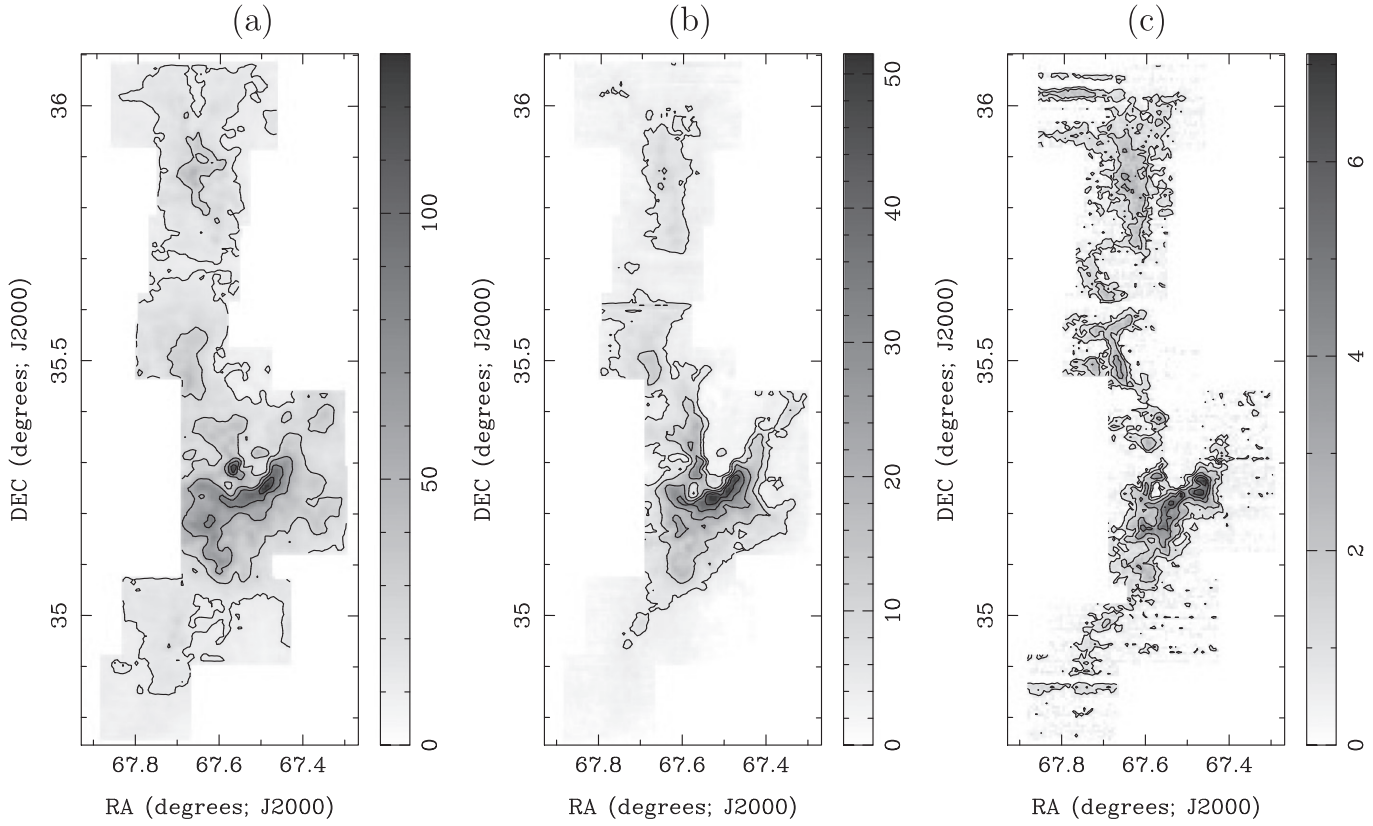

Figure 3. Integrated intensity maps of (a) ^{12}CO(2–1), (b) ^{13}CO(2–1), and (c) C^{18}O(2–1) of the Southeast region of the cloud shown in gray scale with contours overlaid for clarity. The integrated velocity ranges are −12 to 10 km s^{-1}, −10 to 6 km s^{-1}, and −4 to 3 km s^{-1}, respectively. The maximum integrated intensities are 130.0, 51.5, and 7.1 K km s^{-1} for (a) ^{12}CO(2–1), (b) ^{13}CO(2–1), and (c) C^{18}O(2–1), respectively. The contour levels are 10%, 20%, 40%, 60%, and 80% of the maximum of the respective maps. All the maps have been placed on the same spatial grid with a resolution of 38″ sampled at 19″. See the text for more details.

where σ_c (in K) is the rms noise per channel derived for emission-free velocities, and ΔV is the velocity width over which the integrated intensity is calculated. $N_{\rm channel}$ here is the number of real independent channels or filters (of bandwidth 0.25 MHz, ∼0.34 km s^{-1}) within ΔV. The estimated σ_W for ^{12}CO(2–1), ^{13}CO(2–1), and C^{18}O(2–1) integrated intensity maps are 0.16, 0.22, and 0.16 K km s^{-1}, respectively. We also calculated the rms for an integrated intensity map computed over the same number of emission-free channels in the data cube. The σ_W derived this way are 0.11, 0.24, and 0.24 K km s^{-1}, respectively. To be conservative, we adopt the larger value for σ_W, i.e., 0.16, 0.24, and 0.24 K km s^{-1} for ^{12}CO (2–1), ^{13}CO(2–1), and C^{18}O(2–1), respectively (hereafter $\sigma_{W,12}$, $\sigma_{W,13}$, and $\sigma_{W,18}$). The ^{12}CO and ^{13}CO lines are very strong, and in our subsequent analysis we only consider integrated intensities detected above $5\sigma_W$. With C^{18}O, we only consider detections above $2\sigma_W$. We also note some striping apparent in tiles 5, 16, and 17 of the C^{18}O map. These are likely artifacts due to system temperature variations in some of the OTF scans in those regions of the cloud. Prior to the subsequent analysis of these data reported below, this map was "cleaned" so that pixels containing the stripes were removed from the C^{18}O database.[7]

[7] In all cases, the stripes show up in only one polarization. We masked them before combining the two polarization maps. The striping area would therefore have higher noise (by a factor of 1.4).

3.3. CO Excitation and Column Densities of ^{13}CO and C^{18}O

In this paper we adopt the standard LTE analysis to determine excitation temperatures and column densities. The main-beam brightness temperature, $T_{\rm mb}$, is given by

$$T_{mb} = \left[J_\nu\left(T_{ex}\right) - J_\nu\left(T_{bg}\right)\right]\left(1 - e^{-\tau_\nu}\right) \quad (2)$$

where $J_\nu(T) = \frac{h\nu/k}{\left(e^{h\nu/kT} - 1\right)}$ is the Rayleigh–Jeans equivalent temperature of a blackbody of physical temperature T, $T_{\rm ex}$ the excitation temperature of the line under consideration, $T_{\rm bg}$ the temperature of the background (in this case the cosmic microwave background), and τ_ν the optical depth of the transition. The excitation temperature $T_{\rm ex}$ of a given line can be derived from the peak temperature of the line, provided that the line is optically thick. Typically ^{12}CO emission is optically thick in GMCs. In the CMC a large opacity for the ^{12}CO(2–1) line is confirmed by the ^{12}CO/^{13}CO integrated intensity ratio. The probability density distribution for this ratio for all pixels is found to peak near a value of 3.5, considerably smaller than the optically thin limit of ≈40–70 (see, e.g., Langer & Penzias 1993). Less than 10% of the pixels are characterized by ratios exceeding 10. This is consistent with the fact that the surveyed area was dominated by relatively high extinction (dust column density). For $\tau \gg 1$, $T_{\rm ex}$ for the ^{12}CO line is calculated from the following equation (by solving

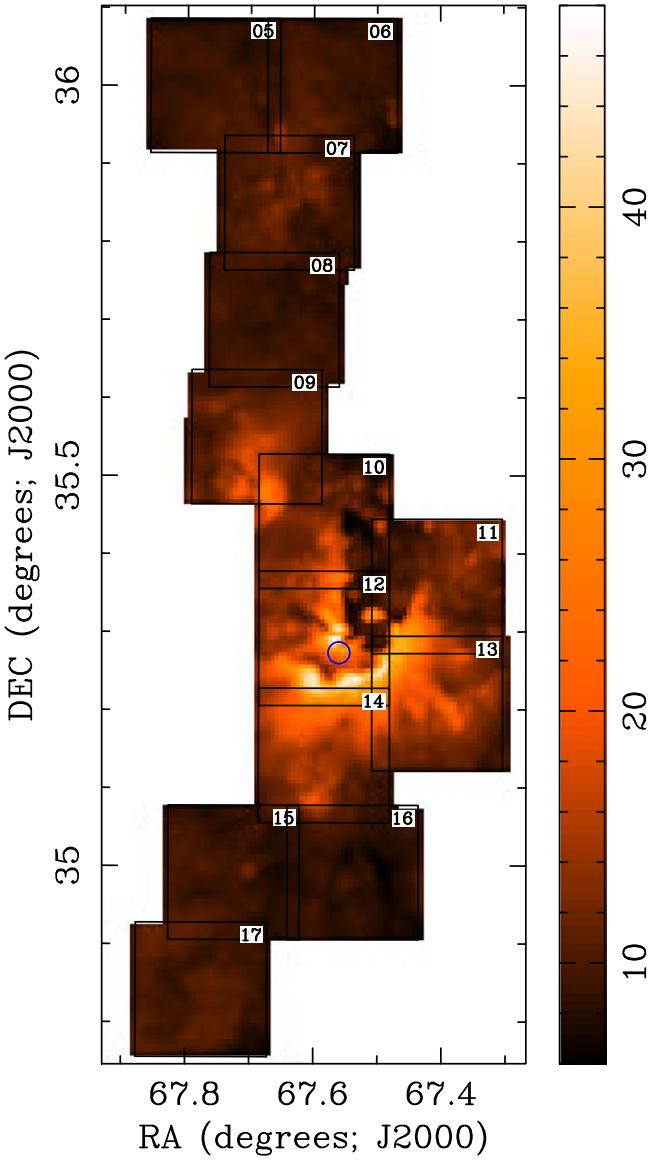

Figure 4. T_{ex} map of the southeast region of the cloud derived from the CO(2–1) map using Equation (3). The boxes show the observed tiles 5–17. The blue open circle shows the position of the LkHα 101 cluster (from SIMBAD).

Equation (2)):

$$T_{ex} = \frac{h\nu/k}{ln\left(1 + \frac{h\nu/k}{T_{\rm mb,p} + J_\nu\left(T_{bg}\right)}\right)} \quad (3)$$

where $T_{\rm mb,p}$ is the peak brightness temperature in the ^{12}CO line. At this frequency, $J_\nu\left(T_{bg}\right) = 0.19$ K and is generally much less than the peak line temperature ($T_{\rm mb,p}$). The typical error[8] in $T_{\rm ex}$ propagated from the 3σ uncertainty in $T_{\rm mb,p}$ is ~0.22 K. The maximum percentage error in $T_{\rm ex}$ is below 5%. Note that in some regions, e.g., tiles 12 and 14, the ^{12}CO line shows self-absorption, and this would result in underestimation of $T_{\rm mb,p}$ and thus $T_{\rm ex}$. For $T_{\rm mb,p}$ between 6 and 50 K, a change of this quantity by 1 K produces a corresponding change of $T_{\rm ex}$ by 1 K.

Figure 4 shows a map of the spatial distribution of the ^{12}CO excitation temperatures in the surveyed region. Over the vast majority of the cloud, $T_{\rm ex}$ is found to be in a narrow range around 10 K as expected for gas heated by cosmic rays and cooled by molecular lines (Goldsmith & Langer 1978; Bergin & Tafalla 2007). Higher temperatures are found in the southern part of the region. The highest excitation temperatures approach 40 K and are found within the bright filamentary ridge southwest of the LkHα 101 cluster (see figure), suggesting that the cluster is providing additional heating of the gas in that area.

The optical depths of ^{13}CO(2–1) (τ_{13}) and C^{18}O(2–1) (τ_{18}) were calculated assuming LTE from

$$\tau = -ln\left[1 - \frac{T_{mb}}{h\nu/k}\frac{1}{\left(e^{\frac{h\nu}{kTex}} - 1\right)^{-1} - \left(e^{\frac{h\nu}{kTbg}} - 1\right)^{-1}}\right]. \quad (4)$$

Here $T_{\rm ex}$ for both transitions was taken to be that derived for ^{12}CO(2–1). The probability density distribution of opacities for ^{13}CO peaks around 0.5 with the majority (87%) of pixels appearing to be relatively optically thin (i.e., $\tau < 1$). For C^{18}O the distribution peaks around 0.2, significantly less than that for ^{13}CO (as expected), and with $\tau < 1$ for essentially all pixels in the map.

We followed Pineda et al. (2010) in calculating both the ^{13}CO and C^{18}O column density using Equation (5) for the $J = 2$–1 transition.[9] The rotational constant B_0 and the Einstein coefficient $A_{2\to1}$ are taken from an online database.[10] The partition function Q is estimated by Equation (6), which is accurate to 10% for $T > 5$ K (note that in our data, $T_{\rm ex} > 5$ K everywhere, as shown in Figure 4):

$$N = \frac{8\pi k\nu^2}{hc^3A_{2\to1}}\frac{e^{\frac{h\nu}{kTbg}} - 1}{e^{\frac{h\nu}{kTbg}} - e^{\frac{h\nu}{kTex}}}\frac{Q}{(2J+1)e^{\frac{-hB0J(J+1)}{kTex}}} \times \frac{\int\tau(v)dv}{\int\left[1 - e^{-\tau(v)}\right]dv}\int T_{mb}dv\,(\mathrm{cm}^{-2}) \quad (5)$$

$$Q \equiv \Sigma_J(2J+1)e^{\frac{-hB_0J(J+1)}{kT_{ex}}} \simeq \frac{kT_{ex}}{hB_0} + \frac{1}{3} \quad (6)$$

We note that sub-thermal excitation for the optically thin ^{13}CO(2–1) and C^{18}O(2–1) lines might be expected to be a concern in low-extinction regions of the cloud where number densities may be lower than the critical density for thermal (LTE) excitation ($\approx 3 \times 10^4$ cm^{-3}). This could lead to underestimates of the CO column densities in the outer regions. However, since the studied area here is dominated by relatively high extinction ($A_{\rm V} \gtrsim$ 3–4 mag), we expect that the effects of any sub-thermal excitation are minimized. We can roughly estimate the magnitude of this effect using the RADEX, non-LTE, radiative transfer code (van der Tak et al. 2007). We find that with $n\left(\mathrm{H}_2\right) = 5 \times 10^3$ cm^{-3}, $T_{\rm gas} = 10$ K, and $W(^{13}\mathrm{CO}) \approx 2.5$ K km s^{-1}, $N_{\rm RADEX} \approx 2.0\, N_{\rm LTE}$.

[8] This value encloses 90% of pixel errors.

[9] We noticed the typo in Equation (18) in Pineda et al. (2010), as pointed out by Ripple et al. (2013).

[10] http://home.strw.leidenuniv.nl/~moldata/CO.html

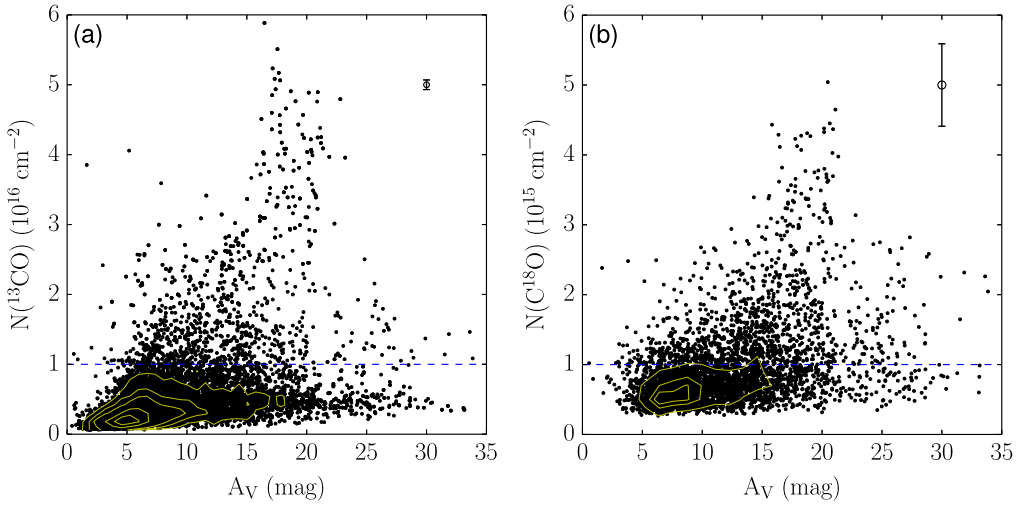

Figure 5. Pixel-by-pixel comparison between (a) ^{13}CO, (b) C^{18}O column density, and visual extinction A_V for the entire surveyed area. Each point represents a 19″ pixel that corresponds to ~0.04 pc at a distance of 450 pc. A $5\sigma_{W,13}$ cut is applied to $W(^{13}CO)$ in the $N(^{13}CO)$ calculation, while a $2\sigma_{W,18}$ cut is applied to $W(C^{18}O)$ in the $N(C^{18}O)$ calculation. The blue dashed lines tentatively divide the points into two groups: an approximately constant abundance group above the line and a constant column density group below. The size of the error bar encloses 90% of the calculated 3σ errors in column density (see the text). The error of A_V is too small to be shown (Section 3.1). See Section 4.1.1.

4. DISCUSSION

4.1. CO Column Densities and Visual Extinction

4.1.1. ^{13}CO and $C^{18}O$ Abundances

Since our measurements of CO column densities and dust extinction are set to the same angular resolution and spatial grid, we are in a position to directly compare the two data sets. We note here that the angular scale of a pixel is 19″, corresponding to a spatial scale of ~0.04 pc (~8000 AU) at a distance of 450 pc (Lada et al. 2009).

Assuming a constant gas-to-dust mass ratio ($N(H)/A_V = 1.88 \times 10^{21}$ cm^{-2} mag^{-1}; Bohlin et al. 1978; Rachford et al. 2009; Pineda et al. 2008), the CO abundance can be expressed as $[CO] = N(CO)/N(H) = N(CO)/[A_V(1.88 \times 10^{21}$ cm^{-2} mag$^{-1})]$. For optically thin emission lines, such as ^{13}CO and C^{18}O, we expect the gas column density to increase linearly with A_V, provided that the cloud is characterized by a constant CO abundance (e.g., Lada et al. 1994; Alves et al. 1999). In Figure 5 we plot the molecular column density versus extinction at each pixel in the mapped region for (a) ^{13}CO and (b) C^{18}O. Contrary to our simple expectations, each plot exhibits considerable scatter with only weak correlations between gas and dust column densities. If the gas in the CMC were characterized by a single, constant abundance, the relation between its column density and extinction would consist of a single straight line in each plot. At fixed A_V there would be only small scatter in N(CO), which is clearly not the case. For instance, at $A_V \sim 20$ mag the ratio between the highest and lowest values of $N(^{13}CO)$ and $N(C^{18}O)$ is $\gtrsim$10 for each isotope. Clearly, the two plots suggest strong spatial variations in abundances of these two species across the cloud.

On closer inspection of Figure 5, one can almost make out two significant branches (correlations) of pixels in both plots. First, a large group of pixels in each plot (below the blue dashed line, i.e., $N(^{13}CO) \lesssim 1.0 \times 10^{16}$ cm^{-2}, $N(C^{18}O) \lesssim 1.0 \times 10^{15}$ cm^{-2}) display an almost constant, low column density across a wide range of A_V. This flat relation between the two quantities indicates a trend of *decreasing* molecular abundance ($[^{13}CO]$ and $[C^{18}O]$) from low to high A_V pixels. Second, another group (above the blue dashed line) of pixels is characterized by gas column densities that appear to rise more or less linearly with extinction to very high column density at $A_V \sim 20$ mag (1.0×10^{16} cm$^{-2} \lesssim N(^{13}CO) \lesssim 6.0 \times 10^{16}$ cm^{-2}, 1.0×10^{15} cm$^{-2} \lesssim N(C^{18}O) \lesssim 6.0 \times 10^{15}$ cm^{-2}), indicating a more or less uniform molecular abundance with depth into the cloud for this group of pixels. These branches likely mark two limiting extremes of spatially dependent variation in the chemical conditions within the CMC.

Spatial variations in ^{13}CO abundances have been reported previously in a few other molecular clouds, although in these clouds the variations appear less pronounced than found here. For the Perseus molecular cloud, Pineda et al. (2008) found generally tighter correlations of ^{13}CO column density with extinction than found here, although they explored the correlation at much lower extinctions (i.e., $A_V \lesssim 10$ mag) than in this study. Nonetheless, over this lower extinction range they did find measurable variations (at the ~40% level) in the abundances with position across the cloud. For the Orion A molecular cloud, Ripple et al. (2013) measured abundances at both low and high extinction and found more significant positional variations in the ^{13}CO abundance across the cloud than observed in Perseus (Pineda et al. 2008). At $A_V \sim 20$ mag, $N(^{13}CO)$ in Orion A was found to vary by about a factor of 4 between various locations in the cloud. Further, Ripple et al. (2013) were able to associate these positional variations in abundance with positional variations in the physical conditions within the cloud. At the lowest extinctions ($A_V \lesssim 3$ mag), where there is not enough ^{13}CO to self-shield against UV dissociation, they found extremely low ^{13}CO abundances with significant (factor of 8) spatial variations. At intermediate extinctions ($3 \lesssim A_V \lesssim 10$ mag), where self-shielding is considerably more effective, higher abundances were found with modest (factor of 2) spatial variations. At the highest extinctions they observed the highest abundances but also the largest spatial variations in abundances across the cloud. The latter regime included cold portions of the cloud where CO depletion depressed the

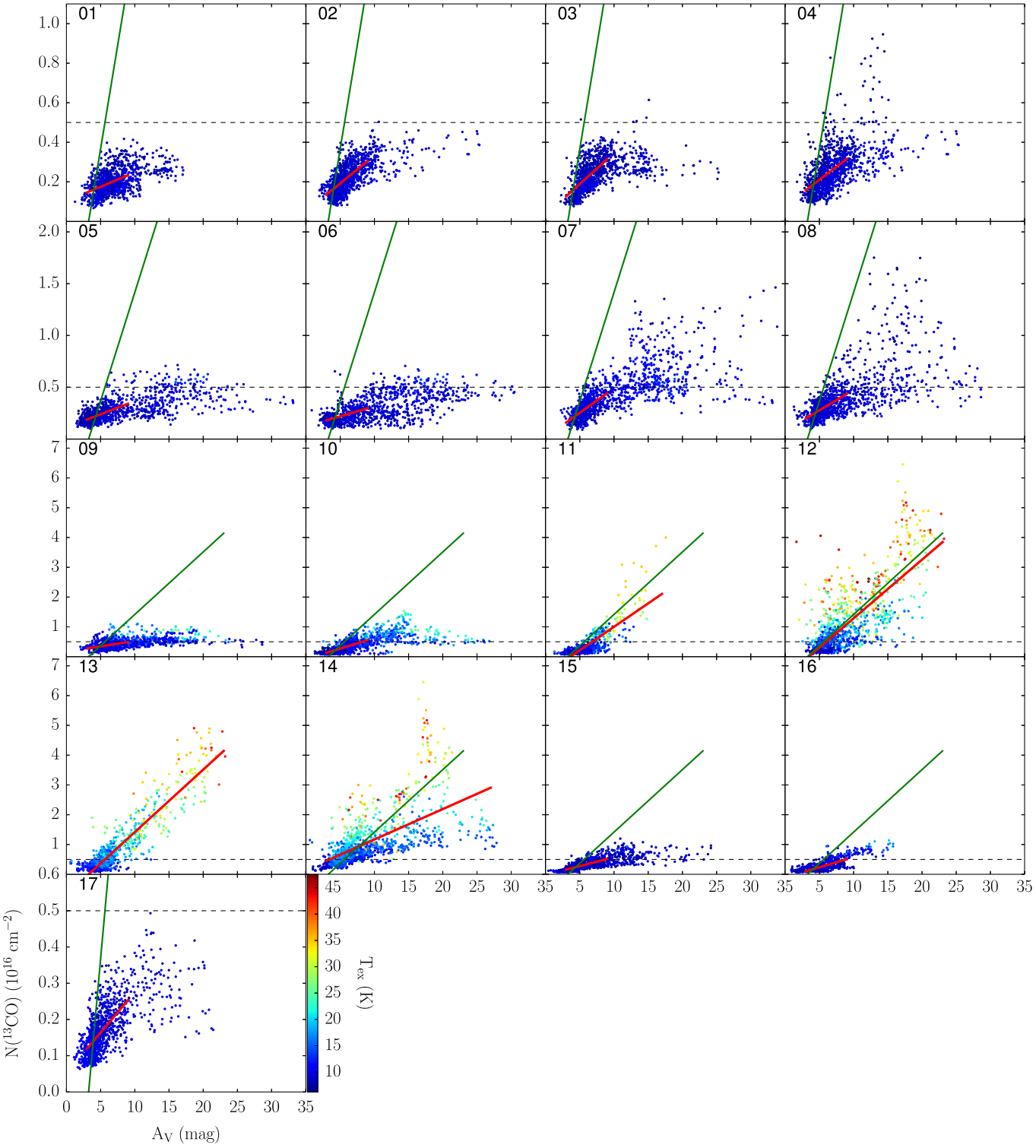

Figure 6. Pixel-by-pixel comparison between ^{13}CO column density and A_V within each tile. The scale of the column density axis varies between tile rows, and a fiducial horizontal line representing a constant $N(^{13}\mathrm{CO})$ of 0.5×10^{16} cm^{-2} is drawn for intercomparison. The individual points are color-coded by T_{ex}. A $5\sigma_{W,13}$ cut is applied to $W(^{13}\mathrm{CO})$ in the $N(^{13}\mathrm{CO})$ calculation. The red solid lines show linear regression in $A_V > 3$ mag for tiles 11–14, and in 3 mag $< A_V <$ 10 mag for the rest. As a reference, the fitting result for tile 13 is shown as green lines in every tile. The magnitude of the error is the same as in Figure 5(a).

abundances, as well as hot regions heated by young stars where CO desorption produced enhanced CO abundances.

4.1.2. Mapping Spatial Variations in CO Abundances

The molecular abundance is regulated by the physical and chemical conditions in the GMC. For instance, the gas-phase molecules can condense onto dust grains to form ice mantles, and the molecules on grain surfaces can be returned to the gas via thermal evaporation (e.g., van Dishoeck et al. 1993; Caselli et al. 1999). These processes are tightly linked to the local temperature (especially the dust temperature) and are responsible for setting the gas-phase molecular abundance. At low

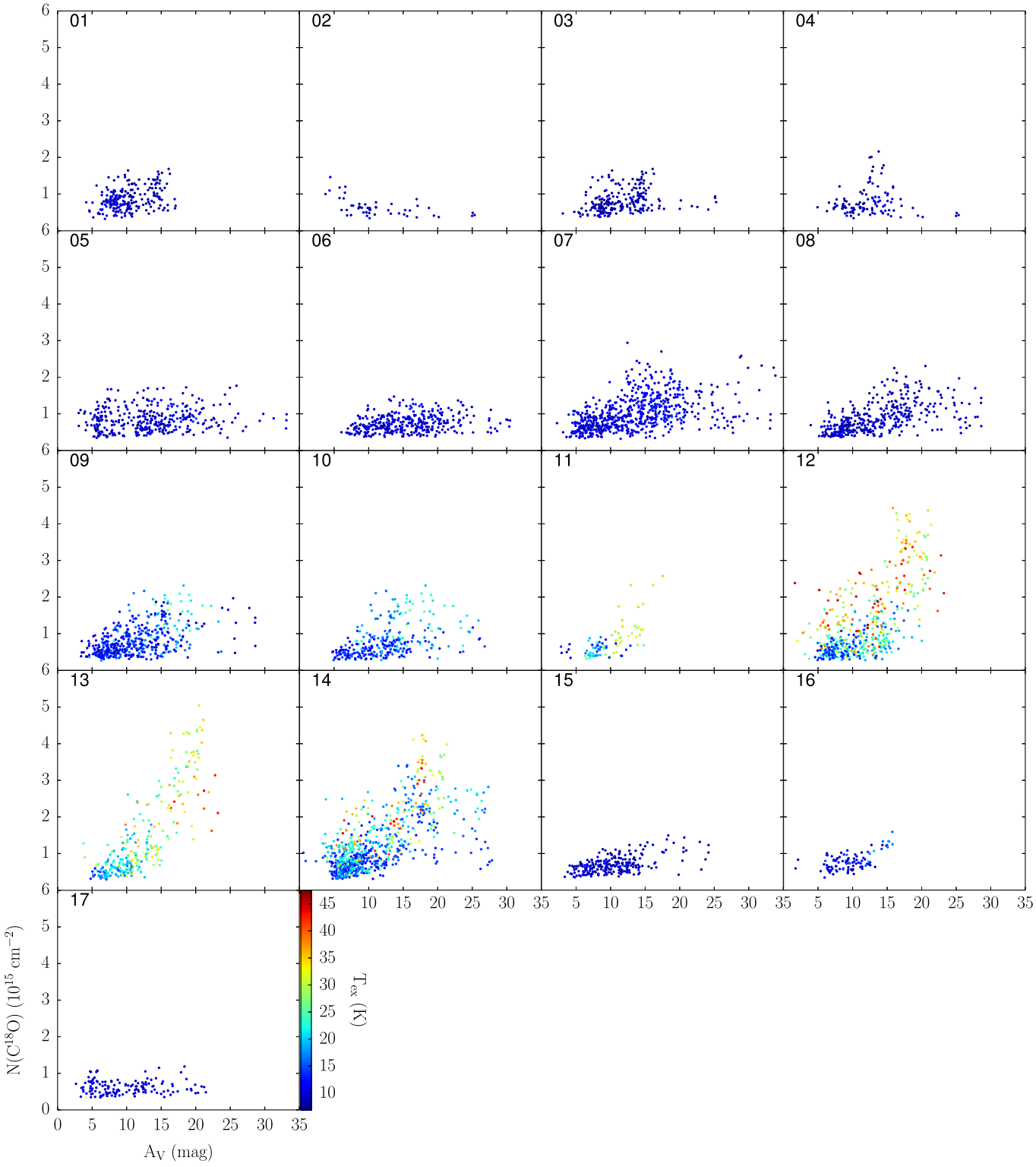

Figure 7. Pixel-by-pixel comparison between $C^{18}O$ column density and A_V within each tile. A $2\sigma_{W,18}$ cut is applied to the integrated intensity in the $N(C^{18}O)$ calculation. The magnitude of the error is the same as in Figure 5(b). The axes have the same horizontal and vertical scales for all tiles; otherwise, the same as Figure 6.

extinctions where column densities of dust and gas are low, abundances are very sensitive to far-UV (FUV) radiation, which can drive volatile chemistry via processes of fractionation and selective photodissociation (Lada et al. 1994; Röllig & Ossenkopf 2013). The large scatter in Figure 5 could plausibly be caused by strong variation of such physical/chemical conditions in different sub-regions of the surveyed area of the cloud. If this is the case, we would expect to observe a tighter correlation between column density and A_V if we restricted the plots to cover smaller spatial areas within the surveyed region,

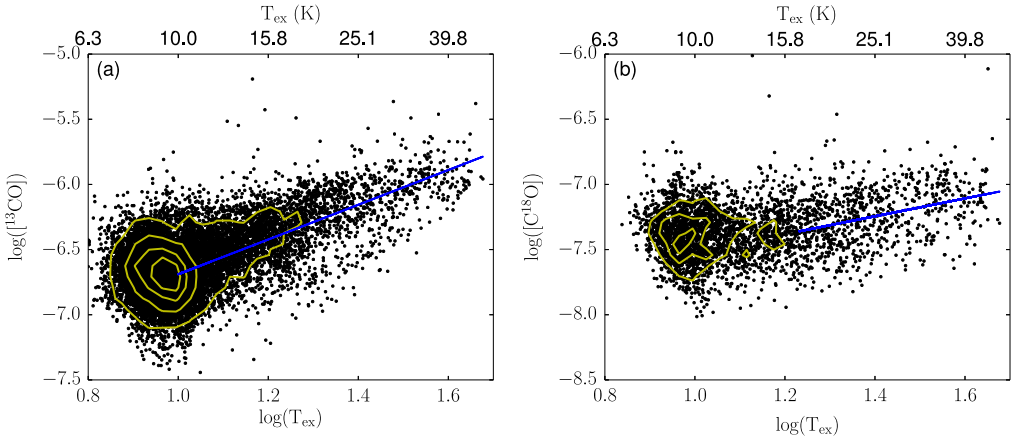

Figure 8. Pixel-by-pixel comparison between (a) ^{13}CO, (b) C^{18}O abundance, and T_{ex} for the entire surveyed area. Each point represents a 19″ pixel that corresponds to ~0.04 pc at a distance of 450 pc. Abundances were calculated from pixels where $W(^{13}\mathrm{CO}) > 5\sigma_{W,13}$ and $W(\mathrm{C}^{18}\mathrm{O}) > 3\sigma_{W,18}$. The yellow contours show the surface density of points. The blue lines show the linear fitting within $T_{ex} > 10$ K for ^{13}CO and $T_{ex} > 17$ K for C^{18}O. See Section 4.1.3.

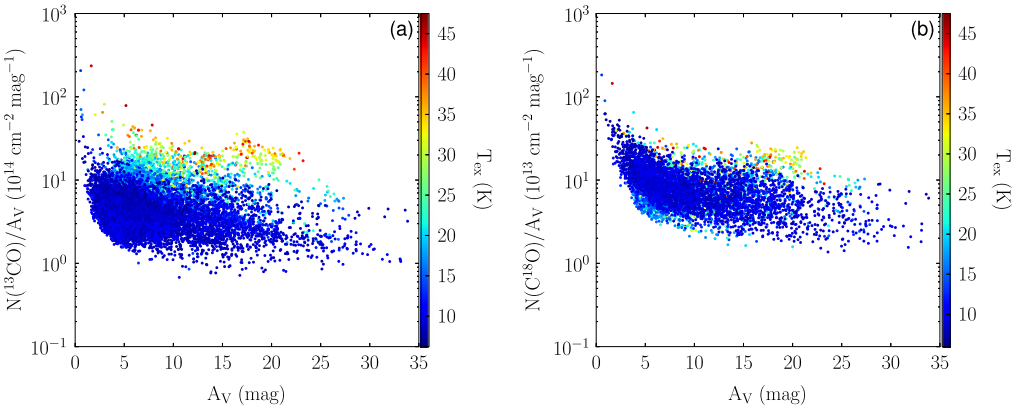

Figure 9. Relation between CO abundance and extinction for (a) ^{13}CO and (b) C^{18}O over the entire surveyed area. Although there is large scatter, both plots show that the abundances of these two rare isotopologues clearly decrease with increasing extinction into the cloud. This is likely a result of CO depletion in the cold, high-extinction regions of the cloud. The individual points are color-coded by the value of the T_{ex} derived from ^{12}CO observations at their position. Note that the hotter pixels have elevated abundances compared to the cold pixels and these abundances do not appear to decrease with extinction.

since the physical conditions in such smaller regions would be expected to be more uniform. Indeed, Ripple et al. (2013) demonstrated the connection between such physical conditions and spatial CO abundance variations in the Orion cloud.

In order to examine the distributions of $N(^{13}\mathrm{CO})$ and $N(\mathrm{C}^{18}\mathrm{O})$ versus A_V on smaller spatial scales, we constructed these relations for each individually observed $10' \times 10'$ mapping tile (see Figures 1 and 2). In Figures 6 and 7 we plot the results for ^{13}CO and C^{18}O, respectively. In the individual plots contained within these figures we indeed see a significant reduction in scatter compared to that characterizing Figure 5. More importantly, there is very strong spatial variation in the relation between extinction and CO column density across the surveyed region of the CMC. This is evident in Figure 6 where we plot linear fits to the data. The results of the fits are shown in Table 2 where the slopes vary by nearly an order of magnitude across the cloud. This is also readily apparent in Figure 7, where the axes on the plots have the same scaling, and especially clear on close inspection of Figure 6, where the scale of the vertical axis ranges by as much as an order of magnitude between the various tiles. These spatial variations in $N(^{13}\mathrm{CO})$ and $N(\mathrm{C}^{18}\mathrm{O})$ give rise to the large dispersion in these quantities in the merged relation constructed for the entire observed region as in Figure 5. Despite the variation in the range of column densities at different locations across the cloud, the range in extinction spanned by the observations in all the plots is very nearly the same. The large variation of column density of ^{13}CO and C^{18}O with dust extinction confirms that the abundances of the two isotopologues exhibit large spatial variations. Consider Figure 6. The tiles can be placed into two groups, one containing tiles 1–10 and 15–17, and the other consisting of tiles 11–14. In the former group, $N(^{13}\mathrm{CO})$ rarely exceeds (5–6) $\times 10^{15}$ cm^{-2}, while in the latter group $N(^{13}\mathrm{CO})$ can reach values as high as (3–5) $\times 10^{16}$ cm^{-2} over the same extinction range. The $N(\mathrm{C}^{18}\mathrm{O})$ plots in Figure 7 exhibit similar behavior.

4.1.3. The Relation between Gas Temperature and CO Abundances

From comparison of Figures 7 and 6 with Figure 4 we see that the tiles (11–14) with the largest values of CO column density spatially coincide with the region of elevated ^{12}CO excitation temperature. Since the ^{12}CO(2–1) line is generally so optically thick, and since our sampled region preferentially contains high column density ($A_V \gtrsim 3$–5 mag) gas, sub-thermal excitation of ^{12}CO is unlikely. Therefore, the excitation temperature map traces the gas kinetic temperature, and the distribution of the molecular abundances [^{13}CO] and [C^{18}O] is tightly related to local physical conditions, in

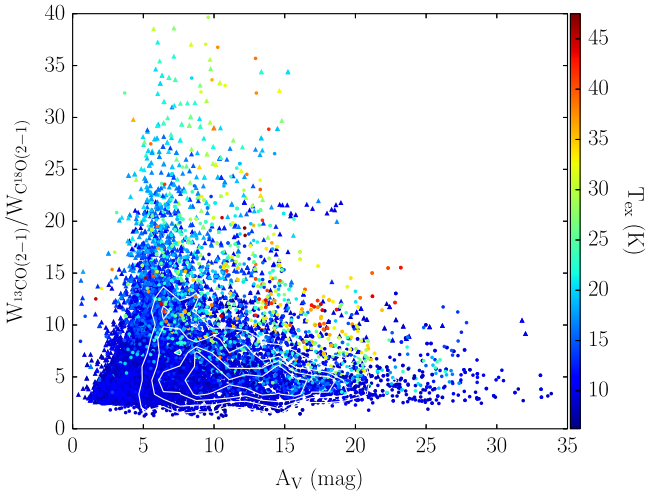

Figure 10. Ratio of $W_{^{13}CO(2-1)}$ and $W_{C^{18}O(2-1)}$ plotted as a function of A_V. $W_{^{13}CO(2-1)}$ is everywhere $>5\sigma_{W,13}$. Those pixels with $W_{C^{18}O(2-1)} > 2\sigma_{W,18}$ are plotted as filled circles; those originally with $W_{C^{18}O(2-1)} < 2\sigma_{W,18}$ are set to have $W_{C^{18}O(2-1)} = 2\sigma_{W,18}$ to reduce scatter in the diagram and are plotted as triangles. These points are all significant lower limits to the true values of the ratio. The white contours show the surface density of pixels with detections. At low extinctions ($A_V \lesssim 15$ mag) there is a large spread in the observed ratios with the largest values (~30–40) considerably in excess of the solar abundance ratio of 5.5. At high extinctions ($A_V \gtrsim 15$ mag) the dispersion in the observed ratios is dramatically less and the ratios are close to the solar value. See Section 4.1.5.

particular the gas kinetic temperature. As a further test of the connection between column density and temperature, we have color-coded the points in Figures 6 and 7 according to the gas temperature in each individual pixel. Inspection of the figures shows that the pixels with the highest gas temperatures ($T_{ex} \gtrsim 15$ K) are also the pixels with the largest CO column densities. Pixels with low gas temperatures ($T_{ex} \lesssim 15$ K) rarely reach high CO column densities, independent of extinction. These correlations imply that the abundances of ^{13}CO and C^{18}O are physically related to the gas temperature distribution.

To examine more directly the relation between the molecular abundances and the gas temperature, we plot the log([^{13}CO]) –log(T_{ex}) relation and log([C^{18}O])–log(T_{ex}) relation in Figure 8. Both molecular abundances show dependence on T_{ex}, although [^{13}CO] is apparently sensitive to T_{ex} over a larger range of temperature than [C^{18}O]. This confirms that [^{13}CO] and [C^{18}O] are both regulated by gas temperature, but over different ranges of temperature in the extinction range (3 mag $\lesssim A_V \lesssim$ 25 mag) we observed. To quantify the relations, we empirically fit a power-law function to the unbinned data for both correlations. T_{ex} is derived from the ^{12}CO line, which has very good S/N. Since the noise of the extinction map is relatively small, i.e., 0.05 mag for $Av < 10$ mag and 0.1 mag for $Av \geqslant 10$ mag, uncertainties in the abundances are dominated by the noise in the molecular line data.

The fits were performed over different ranges of T_{ex} for the two lines: $T_{ex} > 10$ K for ^{13}CO and $T_{ex} > 17$ K for C^{18}O. The low-temperature cutoffs were empirically chosen, by inspection, to correspond to the ranges where the relations appeared to be linear. However, it did not escape our attention that the low-temperature cutoff for C^{18}O corresponds to the CO sublimation temperature of ~17 K (van Dishoeck & Black 1988), and as discussed later, this may not be coincidental. The linear regression gave the following results: [^{13}CO] $\propto T_{ex}^{1.33}$ with correlation coefficient = 0.66; [C^{18}O] $\propto T_{ex}^{0.69}$ with correlation coefficient = 0.34. We performed a χ^2 test on the power-law model for [^{13}CO]–T_{ex} and [C^{18}O]–T_{ex} relations. The χ^2 is calculated using

$$\chi^2 = \Sigma \frac{(O-E)^2}{\sigma_a^2} \quad (7)$$

where O and E stand for observed and modeled [CO] (calculated from the fitted power law), respectively, and σ_a the local standard deviation derived in a 2 K bin enclosing the data. At a significance level of 0.05, the fitted power-law models for [^{13}CO]–T_{ex} and [C^{18}O]–T_{ex} relations are acceptable, and the χ^2 per degree of freedom are 1.02 and 1.06 for [^{13}CO] and [C^{18}O], respectively, meaning that the fit is reasonable. The implications of these results will be discussed in the next two sections of the paper.

4.1.4. Molecular Depletion and Desorption

We argue here that the dependence of the ^{13}CO and C^{18}O abundances on gas temperature shown in Figure 8 is a result of the combined effects of gas depletion and desorption in the CMC. Theoretical considerations suggest that sticking of CO onto dust grains can remove the molecule from gas phase very efficiently within cold ($T < 17$ K) and dense ($n(H_2) > 10^4$ cm^{-3}) regions of molecular clouds (see, e.g., van Dishoeck et al. 1993). Indeed, compelling observational evidence for reduction of [C^{18}O] has been reported for numerous cold ($T < 10$ K) and high-extinction ($A_V \gtrsim 10$ mag) regions of molecular clouds (e.g., Lada et al. 1994; Alves et al. 1999; Caselli et al. 1999; Kramer et al. 1999; Bergin et al. 2001, 2002). Both the radial stratification of the clouds (e.g., Alves et al. 1998, 2001; Bergin et al. 2001) and the presence of emission from high dipole molecules such as NH_3 from such regions indicate that they likely correspond to sufficiently high gas volume densities (>10^4 cm^{-3}) to promote CO condensation onto grain surfaces.

In Figure 9 we plot the relation between (a) ^{13}CO and (b) C^{18}O abundance and extinction in the CMC. Although there is a large scatter in both relations, it is clear that the abundances of the two species decline with extinction in a manner consistent with similar abundance reductions seen in other molecular clouds and suggestive of CO freeze-out onto grain surfaces in the interior regions of the cloud. If this decline in abundances at high extinctions is due to freeze-out, we also expect the reduction of the gas-phase abundances to be occurring in the coldest regions of the cloud. In Figure 9 the points are color-coded by the gas temperature, and we see both a preponderance of cold gas in the cloud and a prominent decrease in abundance with extinction for the cold pixels, while the warm pixels show no decrease. This supports the hypothesis that the decline in abundances with extinction in cold regions is largely due to depletion. Of course, depletion requires low dust temperature, and our analysis has been based on measurements of gas temperature. Gas temperature generally tracks dust temperature (e.g., Forbrich et al. 2014), but direct observations of dust temperature would make for a more compelling case. Fortunately, published maps of dust temperature for the CMC based on *Herschel* observations exist (Harvey et al. 2013). Comparison with our maps shows generally good agreement between the gas and dust

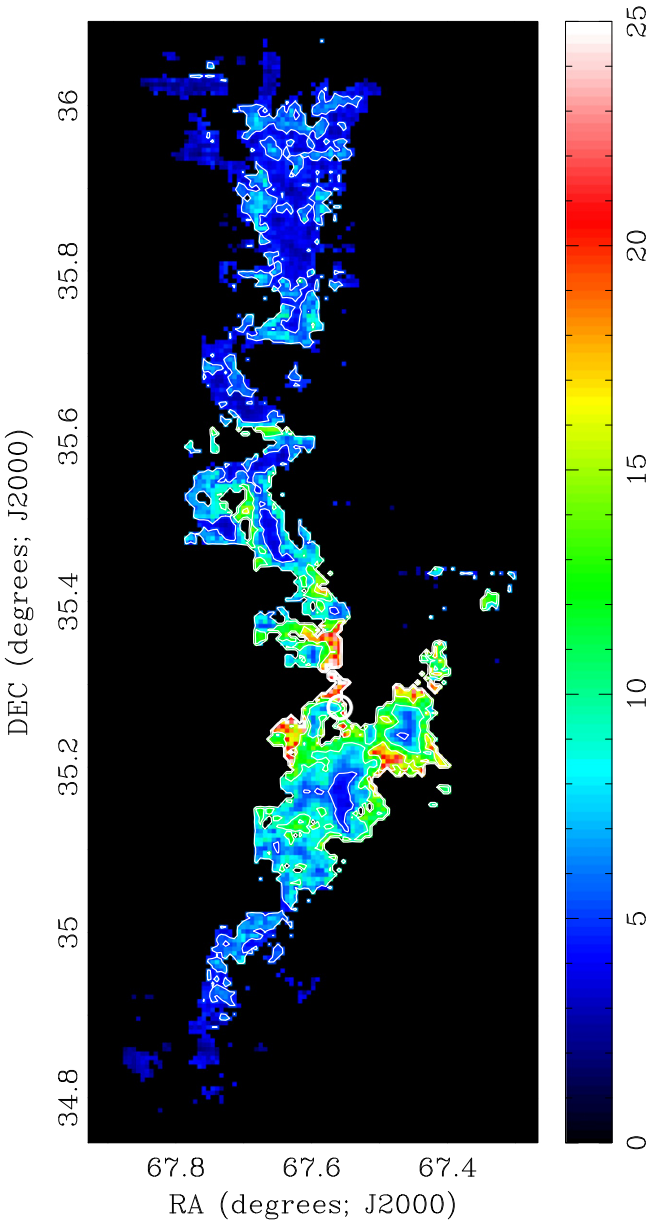

Figure 11. Map of the ^{13}CO-to-C^{18}O integrated intensity ratio in the southern portion of the surveyed region. The contours show $W(^{13}\mathrm{CO})/W(\mathrm{C}^{18}\mathrm{O}) = 5$, 10, and 15. The largest values of this ratio appear in the outer regions where the chemistry is driven by FUV radiation that penetrates deeply into the cloud. It is clear that this effect is larger in the southern region of the map (i.e., $\delta \approx 35°10'$ to $35°20'$), which is in close proximity to the embedded cluster (open white circle) and its UV radiation field, than in the more remote northern portion of the region.

temperature spatial distributions. In particular, in the cold regions away from LkHα 101 (corresponding to our tiles 01–09 and 15–17, respectively), the median $T_\mathrm{d} \sim 14.5$ K and the minimum $T_\mathrm{d} \sim 10$ K (Harvey et al. 2013), far below pure CO ice sublimation temperature (~17 K; van Dishoeck et al. 1993). Under such conditions, Bergin et al. (1995) showed a relatively short CO depletion timescale, $<10^6$ yr. So with $T_\mathrm{d} \sim 10$ K and $n_{\mathrm{H}_2} = 10^4$ cm^{-3}, CO would unavoidably deplete. This is consistent with the reduction of CO abundance we observe in the cold, high-extinction regions in the CMC.

At the higher gas temperatures ($T \gtrsim 17$ K) we would expect that thermal evaporation (desorption) of the gas from the grain surfaces releases any trapped CO and increases its gas-phase abundance relative to the cold regions of the cloud. Indeed, that is what is clearly shown in Figure 8, where the observed abundances increase with increasing gas temperature. The warmest CO gas in our surveyed region is found in four contiguous tiles (11–14) that are in close proximity to the massive star LkHα 101 and its associated cluster (shown as the blue circle in Figure 4). The CMC dust temperature map from Harvey et al. (2013) (see their Figure 4) shows a vast region of high dust temperature ($T_\mathrm{d} \sim 28$ K) near LkHα 101, which coincides with the positions of tiles 11–14 in our observation. It is in this warm area that the CO abundances appear to be at their highest. CO thermal evaporation is caused by high dust temperature. For instance, Bergin et al. (1995) reported that shortly after a "star turns on," the dust temperature reaches $T_\mathrm{d} = 25$ K ($n_{\mathrm{H}_2} = 10^4$ cm^{-3}, $T_\mathrm{gas} = 20$ K), and all CO is in the gas phase within 100 yr. The abundance enhancement near LkHα 101 is likely caused by hot dust heated by the cluster. Over most of the rest of the cloud Harvey et al. (2013) find $T_\mathrm{d} \sim$ 10–14 K. In these regions the gas temperatures are also found to be near 10 K and a significant amount of CO should be locked in ice mantles on the dust grains at least at the highest extinctions (also see Bergin et al. 1995). These considerations suggest that the variation of [^{13}CO] and [C^{18}O] in the CMC is mostly regulated by the chemistry of depletion and desorption, which in turn is driven by the (dust) temperature distribution.

Recently, Ripple et al. (2013) have reported similar results for the Orion A molecular cloud. They divided that cloud into nine spatial partitions (1–9) and considered regions within those partitions with extinctions, $A_\mathrm{V} \gtrsim 5$ mag, similar to those studied here for the CMC. They found that in regions with $5 \lesssim A_\mathrm{V} \lesssim 10$ mag, $N(^{13}\mathrm{CO})$ was generally linearly correlated with A_V. However, in those partitions (2, 3, and 4) that also contained higher-extinction material and were characterized by mean gas excitation temperatures that were below ~22 K, the $N(^{13}\mathrm{CO})$-A_V relation became flat above $A_\mathrm{V} \approx 10$ mag. On the other hand, in two partitions (5 and 6) with both high extinctions and high mean gas excitation temperatures ($T_\mathrm{ex} \sim$ 26–33 K), $N(^{13}\mathrm{CO})$ continued to rise above $A_\mathrm{V} \approx 10$ mag. Ripple et al. (2013) posited that this behavior of $N(^{13}\mathrm{CO})$ with extinction was a result of depletion/desorption effects at $A_\mathrm{V} \gtrsim$ 10 mag. Our results for the CMC are certainly consistent with those of Ripple et al. (2013) for Orion A. In this respect, the physical/chemical conditions in the Orion and the CMC appear to be quite similar. The spatial variations in abundances of the rarer isotopes of CO are largely determined by depletion/desorption effects due to spatial variations in dust (and gas) temperatures resulting from localized star formation activity within the clouds.

4.1.5. The ^{13}CO-to-C^{18}O Abundance Ratio: Influence of UV Photodissociation

In the outer, lower-extinction regions of molecular clouds, FUV radiation is expected to play a role in cloud chemistry (e.g., van Dishoeck & Black 1988; Visser et al. 2009). In low-extinction regions (i.e., $A_\mathrm{V} \lesssim 3$ mag) fractionation of ^{13}CO can increase its abundance relative to ^{12}CO. At somewhat higher extinctions ($A_\mathrm{V} \lesssim 5$ mag) selective photodissociation of C^{18}O is likely to occur due to differences in self-shielding of the FUV intensity at the dissociation wavelengths for the various CO isotopes. The more abundant ^{12}CO and ^{13}CO isotopes are effectively self-shielded at relatively low extinctions ($A_\mathrm{V} \lesssim 1$

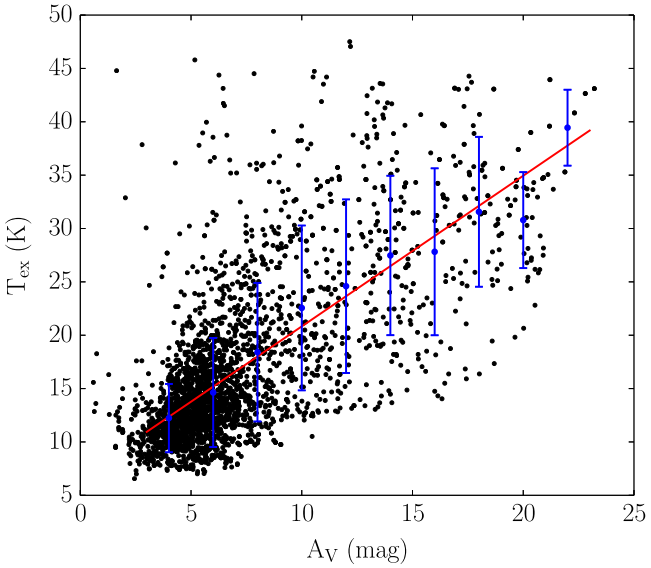

Figure 12. T_{ex}–A_V relation for hot tiles 11–13. The width of the bins is 2 mag. The red solid line shows linear fitting on the unbinned data points. This shows the correlation between T_{ex} and A_V in the region near LkHα 101. Typical errors in T_{ex} are always below 5%. Typical uncertainties in A_V are between 0.05 and 0.1 mag. See the text.

mag), but because the dissociation wavelength of $C^{18}O$ is slightly shifted compared to ^{12}CO and ^{13}CO, and its abundance is relatively low so it is not as effectively self-shielded as the main isotopes, FUV radiation can penetrate deeper into the cloud and dissociate the $C^{18}O$ (Visser et al. 2009). Since our surveys cover relatively high extinction regions ($A_V \gtrsim 5$ mag), we would not necessarily expect selective photodissociation to strongly effect the ^{13}CO- to-$C^{18}O$ abundance ratios. However, earlier studies of Lada et al. (1994) and Shimajiri et al. (2014) suggest that the effects of selective photodissociation may be present at much higher extinctions.

In Figure 10 we plot the ratio of integrated intensities, $W(^{13}CO)/W(C^{18}O)$, as a function of extinction. This ratio is proportional to the abundance ratio for the two species for optically thin lines. It has been shown to be sensitive to the effects of UV radiation on cloud chemistry and abundances (e.g., Lada et al. 1994; Shimajiri et al. 2014). For a solar abundance and optically thin lines, the ratio should be equal to about 5.5 and one would expect the points to scatter around this value, independent of extinction, provided that the cloud is characterized by a constant relative abundance throughout and that the excitation of the two species is not too different. Although at lower extinctions ($A_V \lesssim 15$ mag) there indeed appears to be no obvious correlation between this ratio and extinction, the observed values scatter over an enormous range (≈0–40). The highest values of the ratio exceed the solar value by nearly an order of magnitude.[11] In contrast, at high extinctions ($A_V \gtrsim 15$ mag) the relation is relatively flat with a relatively low dispersion, as might be expected for a constant abundance ratio, and is centered at a value (approximately 4.5) near but somewhat less than the solar value. This behavior does not appear to depend on gas temperature (see figure) and thus is not likely a result of depletion or desorption processes on grains. It is more likely indicative of an active chemical processing of $C^{18}O$ by FUV radiation in regions where $A_V \lesssim 15$ mag. The scatter in Figure 10 is so large at these extinctions because the relative abundance of ^{13}CO and $C^{18}O$ is highly unstable, possibly due to the stochastic variations in FUV flux resulting, in turn, from such factors as the cloud structure and geometry and nature of the external radiation field.

In Figure 11 we show a map of the distribution of the integrated intensity ratio over the southern portion of the CMC. Examination of this map shows systematically increasing values of the integrated intensity ratio at the edges of the cloud with the material nearest the star LkHα 101 exhibiting the largest center-to-edge increases in the ratio. The latter region appears to contain a well-developed photon-dominated region (PDR), while the dense cloud material to the north is much more quiescent in this regard. In their study of the Orion cloud Shimajiri et al. (2014) reported averaged values of the ^{13}CO- to-$C^{18}O$ integrated intensity ratio ranging from about 10 to 17 in the seven PDRs they observed in that cloud. Moreover, they also found the variations in this ratio to be linked to variations in the external FUV radiation field.

In the inner, higher-extinction regions of the CMC, where FUV photons cannot penetrate, the abundances are more chemically stable and apparently somewhat below the solar value. Our observations do indicate, however, that FUV photons are present at relatively large (projected) depths ($A_V \sim 15$ mag) in the cloud, confirming results from earlier studies (e.g., Lada et al. 1994; Shimajiri et al. 2014).

We now address the earlier observation that the relations between the CO abundances and temperature (Figure 8) show positive correlations but over different temperature ranges. One might have expected both ^{13}CO and $C^{18}O$ molecules to show abundances that increased with temperature over similar temperature ranges, since their binding energies are very similar. However, the difference may result from the effects of selective UV dissociation of $C^{18}O$.

In the CMC we also find T_{ex} to be correlated with A_V in regions where warm gas is present. Figure 12 displays the relation between T_{ex} and A_V for the warm tiles (11–13) in our map. Although the scatter is large at high A_V, there is no doubt of a strong trend between the two quantities with $T_{ex} \propto A_V$. Interestingly in this region the temperature reaches the CO sublimation temperature at roughly $A_V = 6$–7 mag. Therefore, it is possible that, even though $C^{18}O$ is being evaporated from grains at $A_V \gtrsim 6$ mag (where $T_{ex} \gtrsim 17$ K), it is also being selectively photodissociated by deeply penetrating UV radiation until depths of $A_V \sim 15$ mag. For larger values of A_V, dust absorption effectively removes the dissociating UV radiation, and higher gas (dust) temperatures associated with this region liberate more $C^{18}O$ from grain surfaces. Indeed, the $C^{18}O$ abundances at these higher extinctions and temperatures may reach levels that also allow some $C^{18}O$ self-shielding. Consequently, $C^{18}O$ does not reach the expected levels of increased abundance due to evaporation from grains until cloud depths are sufficient to shield the molecule from UV radiation. Because of its higher abundance, ^{13}CO self-shields at much lower cloud depths and the effects of its increased abundance,

[11] We note here that in the outer regions of the cloud, $C^{18}O$ is often undetected while ^{13}CO is still quite strong. Because $C^{18}O$ is in the denominator, the ratio is very sensitive to noise in the outer regions. However, at all locations ^{13}CO detections exceed the 5σ level. To reduce the scatter in the plot due to non-detections of $C^{18}O$, we set the $C^{18}O$ integrated intensity equal to 2 $\sigma_{W,18}$ for those pixels where $W(C^{18}O)$ is below 2 $\sigma_{W,18}$. We represent the resulting lower limits on the calculated ratio as triangles in the plot (see the figure).

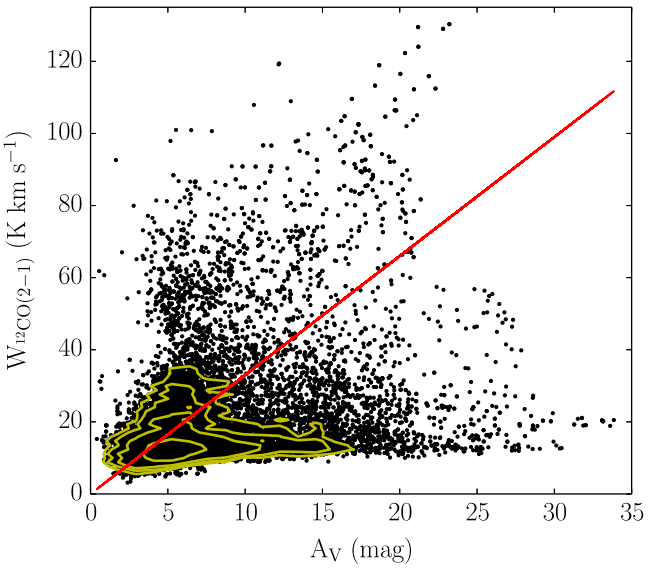

Figure 13. Pixel-by-pixel comparison between ^{12}CO(2–1) integrated intensity and visual extinction A_V for the entire surveyed area. Each point represents a 19″ pixel that corresponds to ∼0.04 pc at a distance of 450 pc. The red solid line represents the standard Milky Way X_{CO} with a slope of 3.3 (K km s^{-1}) mag^{-1}. The yellow contours show the surface density of points. Uncertainties are comparable to or less than the size of the symbols. See Section 4.2.

due to evaporation from grains, are observed at lower extinctions (and corresponding lower temperatures) than C^{18}O.

4.2. X(CO) on Sub-parsec Scales

Even though H_2 is the dominant constituent of molecular clouds, ^{12}CO emission is the most accessible tracer of such gas in the interstellar medium (ISM). It is often the only molecular tracer that can be readily detected in distant clouds and galaxies and consequently has been used to estimate the mass of the molecular component of the ISM in these systems (e.g., Bolatto et al. 2013). To make such estimations requires knowledge of the so-called *X*-factor, that is, the CO conversion factor,

$$X_{CO} = N(H_2)/W(CO_{J=1-0}) \quad (8)$$

The standard determination of this factor is via use of virial theorem techniques (e.g., Solomon et al. 1987). However, the most straightforward way to determine the *X*-factor is by comparing direct measurements of CO and A_V on sub-parsec scales in local clouds. Traditionally this is accomplished by measuring the slope of the correlation between the two quantities at low extinctions ($A_V < 5$ mag) where the CO appears to be effectively thin (e.g., Dickman 1978; Frerking et al. 1982; Lombardi et al. 2006). We adopt a slightly different approach and use all our observations to compute a global or average *X*-factor for the CMC cloud, that is, $\langle X_{CO(1-0)}\rangle = \langle N(H_2)\rangle/\langle W(CO)\rangle = 2.53 \times 10^{20}$ cm^{-2} (K km s^{-1})$^{-1}$. This value is 25% larger than the standard Milky Way value but within the range of values derived for individual molecular clouds in other studies (e.g., Bolatto et al. 2013). Another approach is to derive the on-the-spot X_{CO}, that is, we evaluate Equation (8) at each pixel in our map and obtain $\langle X_{CO(1-0)}\rangle_{ots} = <N(H_2)/W(CO)> = 3.1 \times 10^{20}$ cm^{-2} (K km s^{-1})$^{-1}$. The former $\langle X_{CO}\rangle$ is equivalent to the latter weighted by the integrated intensity.

However, both recent observational studies (Pineda et al. 2008, 2010; Bieging et al. 2010; Ripple et al. 2013; Lee et al. 2014) and numerical simulations (Shetty et al. 2011a, 2011b) have shown that X_{CO} can be strongly dependent on local physical conditions. Since the CMC displays a wide range of physical conditions (e.g., temperature, star formation activity, and spatially variable CO abundances), it would be interesting to measure both X_{CO} and its internal variation on sub-cloud, sub-parsec scales.

To do this, we first performed the traditional pixel-by-pixel comparison between $W_{^{12}CO(2-1)}$ and A_V for the entire surveyed region, as shown in Figure 13. Assuming a constant gas-to-dust ratio $N(H_2)/A_V = 9.4 \times 10^{20}$ cm^{-2} mag^{-1} (Bohlin et al. 1978; Rachford et al. 2009; Pineda et al. 2008) and a constant line-integrated intensity ratio $W_{CO(2-1)}/W_{CO(1-0)} = 0.7$, $X_{CO(1-0)}$ is inversely proportional to $W_{^{12}CO(2-1)}/A_V$ in the plot. In the Milky Way disk, the typical value is $X_{CO(1-0)} \sim 2 \times 10^{20}$ cm^{-2} (K km s^{-1})$^{-1}$ (e.g., Bolatto et al. 2013). This implies a reference value $A_V/W_{CO(2-1)} \approx 0.30$ (K km s^{-1})$^{-1}$ mag. We plot a red line indicating this reference value in Figure 13, with a slope of $W_{CO(2-1)}/A_V \approx 3.3$ (K km s^{-1}) mag^{-1}. At fixed A_V, a point above this line indicates a smaller $X_{CO(2-1)}$, and vice versa.

We can see significant scatter in this plot indicating significant spatial variations in $X_{CO(2-1)}$ on pixel or sub-parsec spatial scales. In order to investigate the spatial dependence of $X_{CO(2-1)}$, we determined the $W_{^{12}CO(2-1)}$–A_V relation in each individual tile of our CO survey, following Section 4.1.2. These relations are shown in Figure 14. There are several familiar features of these plots that are similar to what we have seen in Figure 6, i.e., less scatter in the relations within the individual tiles, systematic spatial variations in the $W_{^{12}CO(2-1)}$–A_V relation across the cloud, and good correlation between high $W_{^{12}CO(2-1)}$ and high gas temperature ($T_{ex} \gtrsim 15$ K).

The general similarity[12] in the behavior of $W_{^{12}CO(2-1)}$ and $N(^{13}CO)$ with extinction is perhaps surprising given that the ^{12}CO emission is very optically thick while ^{13}CO emission is considerably less thick and mostly optically thin. Since N(^{13}CO) is proportional to $W_{^{13}CO(2-1)}$, consider that in this situation $W_{^{13}CO(2-1)} \approx \left[J_\nu(T_{ex}) - J_\nu(T_{bg})\right] \times \tau_\nu^{13} \Delta v_{13}$, while $W_{^{12}CO(2-1)} \approx \left[J_\nu(T_{ex}) - J_\nu(T_{bg})\right] \times \Delta v_{12}$, where Δv is the line width of the corresponding spectrum. Unlike $W_{^{13}CO(2-1)}$, $W_{^{12}CO(2-1)}$ has no dependence on τ or column density, but it is proportional to T_{ex}, the gas excitation temperature.

Particularly interesting in this regard is the behavior of $W_{^{12}CO(2-1)}$ in tile 13 near where the embedded cluster is heating the cloud. Here, there appears to be a clear linear relation between $W_{^{12}CO(2-1)}$ and A_V to the highest measured extinctions (≈25 mag) despite the fact that the ^{12}CO emission in this region of the cloud is so saturated that it is self-reversed (see Figure 2). Because the CO emission is so optically thick, this behavior must be primarily the result of the gradient of T_{ex} with A_V observed in this region of the cloud (see Figure 12) . This is also evident in Figure 15, which shows an expanded

[12] By "similarity" we mean that the hot tiles 11–14 show steeper slopes than the cold tiles in both $W_{^{12}CO(2-1)}$–A_V (Figure 14) and $N(^{13}CO)$–A_V (Figure 6) relations. The apparent relative differences between the cold tiles in Figure 6 and those in Figure 14 are a result of different *y*-axis scaling.

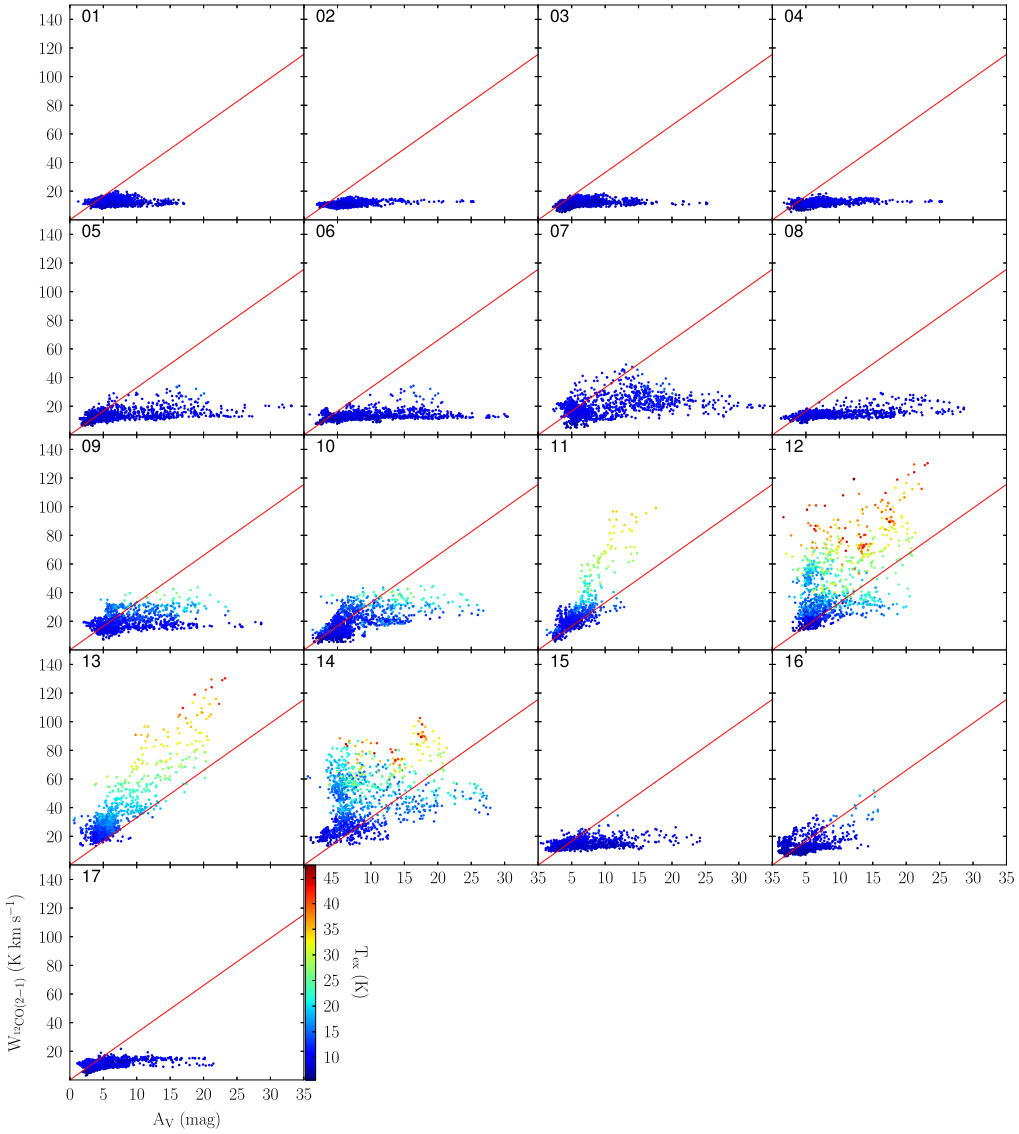

Figure 14. Pixel-by-pixel comparison between ^{12}CO integrated intensity and A_V within each tile. All tiles are shown in the same scale in both axes. The red solid lines represent the standard Milky Way X_{CO} with a slope of 3.3 (K km s^{-1}) mag^{-1}.

view of the $W_{^{12}CO(2-1)}$–A_V relation for tile 13. We can clearly see a temperature gradient in the distribution of color-coded points from low to high A_V. Both W(CO) and T increase by a factor of ~5–6 from low to high A_V. This indicates that the temperature gradient accounts for the bulk of the change in W(CO) with A_V in this region. Of course, other factors could contribute to the increase in W(CO), such as an increase in velocity dispersion with temperature, or even increased [CO] due to desorption as with C^{18}O and ^{13}CO as discussed previously. We do find some evidence for a marginal (35%) increase in the velocity dispersion of the hot gas, but its magnitude is far from sufficient to account for the increased (×6) measures of W(CO). A desorption-induced increase in CO abundance most certainly has occurred in the hot gas, and although the ^{12}CO line is very optically thick, we might expect that additional photons could leak out in the line wings and possibly increase the measured velocity dispersion. But as we already remarked, this effect cannot be significant since the change in peak brightness is observed to be comparable to the change in W(CO) and substantially larger than changes in the velocity dispersion.

Consequently, in the set of tiles near the massive star LkHα 101 (11–14) we conclude that heating of CO enhances $W_{^{12}CO(2-1)}$ in a manner that induces a positive correlation with extinction despite the fact that the emission is saturated. These observations suggest that heating by OB stars produces gradients in the excitation temperature of the CO emitting gas such that in warm regions $W(^{12}CO)$ is proportional to A_V and thus to $N(H_2)$ over a wide range of extinctions. This, in turn, indicates that a single, meaningful X-factor can be derived for these hotter regions using the observations. In Figure 14, tile 13 shows the best correlation between $W(^{12}CO)$ and A_V. We performed a linear regression for tile 13, which is shown in Figure 15. Our result implies

$$X_{CO} \simeq 1.5 \times 10^{20}\ \mathrm{cm^{-2}}\left(\mathrm{K\ km\ s^{-1}}\right)^{-1}$$

in this tile over the range 3 mag $< A_V <$ 25 mag. From the average of the individual, on-the-spot, X_{CO} values in tile 13 we

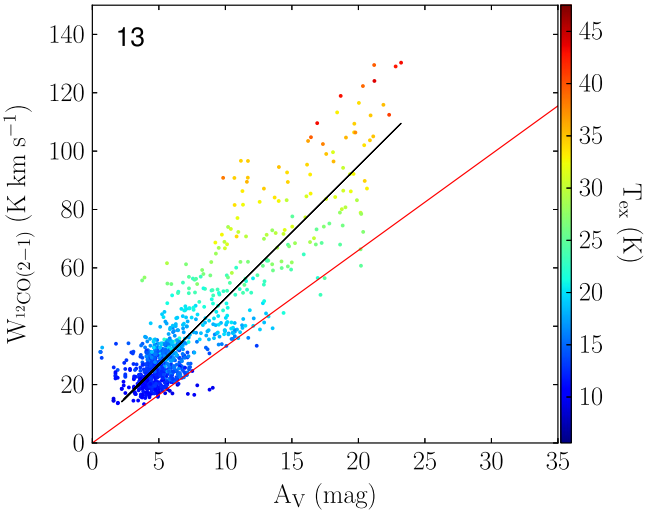

Figure 15. Tile 13 from Figure 14. The black solid line is a linear regression. The fitted slope corresponds to $X_{CO} = 1.5 \times 10^{20}$ cm^{-2}(K km s^{-1})$^{-1}$. The red solid line represents the fiducial Milky Way value, $X_{CO} = 2.0 \times 10^{20}$ cm^{-2}(K km s^{-1})$^{-1}$.

find $\langle X_{CO} \rangle = 1.3 \times 10^{20}$cm^{-2}(K km s^{-1})$^{-1}$, in excellent agreement with the value derived from the linear regression. This clearly supports the idea of a constant value in the hot gas. The derived value is less than both that found for the global average of the CMC and the value (2.0×10^{20} cm^{-2}(K km s^{-1})$^{-1}$) usually adopted for the Milky Way.

This result would suggest that in regions heated by OB stars (e.g., H II regions, extragalactic starbursts), reasonably accurate gas masses could be derived using a standard *X*-factor analysis with a single value of the *X*-factor. Unfortunately, it is not at all clear how one would predict the appropriate value to use in all situations.

However, some clues may be found in the analysis of the regions away from OB stars, where there is only ambient heating of the gas from cosmic rays and the general galactic UV radiation field. Here we observe no correlation between $W_{^{12}CO(2-1)}$ and A_V at modest to high extinctions (i.e., $A_V \gtrsim$ 3–5 mag). This behavior is due to the fact the ^{12}CO line is almost always saturated at high extinctions and the cold gas is very nearly isothermal. Consequently, these cold, quiescent regions are not characterized by a single empirical *X*-factor; instead, the *X*-factor systematically increases with extinction and, in the CMC, is almost always larger than the Milky Way value. This is shown in Figure 16(a), where we plot the relation between the on-the-spot *X*-factor and A_V for the regions of the cloud not heated by the cluster (i.e., tiles 1–10 and 15–17). As expected, there is a clear correlation, and a linear least-squares fit to the unbinned data finds that $X_{CO} \propto N(H_2)^{0.7}$. For the cold tiles we find $\langle X_{CO} \rangle = 3.4 \times 10^{20}$ cm^{-2}(K km s^{-1})$^{-1}$. The (constant) *X*-factor in the hotter regions (e.g., tile 13) has a value considerably lower than those in the cold regions, suggesting that X_{CO} may also increase with decreasing gas temperature within the cloud. Such a trend is clearly evident in our observations and is shown in Figure 16(b), where we plot the relation between the on-the-spot X_{CO} and T_{ex} for the entire cloud. A linear least-squares fit to the (binned) data gives $X_{CO} = 2.0 \times 10^{20}(T_{ex}/10)^{-0.7}$ cm^{-2}(K km s^{-1})$^{-1}$. In this instance we chose to fit the binned data to give greater weight to high-temperature measurements. A fit to the unbinned data gives a slightly steeper slope (−0.9 vs. −0.7).

The observed inverse correlation between X_{CO} and T_{ex} is potentially interesting. It suggests that differences between globally averaged *X*-factors derived for different clouds could be a result of variations in the relative amounts of hot and cold gas within the clouds, provided that their velocity dispersions are similar. Active star-forming clouds with OB stars and H II regions, such as Orion, might be expected to have average *X*-factors that are lower than more quiescent clouds, such as the CMC. Indeed, Digel et al. (1999) derive $X_{CO} = 1.35 \times 10^{20}$ cm^{-2}(K km s^{-1})$^{-1}$ for the entire Orion complex from γ-ray data, in agreement with recent determinations using CO (Ripple et al. 2013). Moreover, γ-ray observations of Orion with the *Fermi* satellite by Ackermann et al. (2012) found that in the (cold) regions removed from the OB stars and H II regions, $X_{CO} = 2.2 \times 10^{20}$ cm^{-2}(K km s^{-1})$^{-1}$, while in the (hotter) parts of the cloud complex associated with the H II regions, $X_{CO} = 1.3 \times 10^{20}$ cm^{-2}(K km s^{-1})$^{-1}$, very similar to what we find in the CMC. For the Taurus cloud, which has no

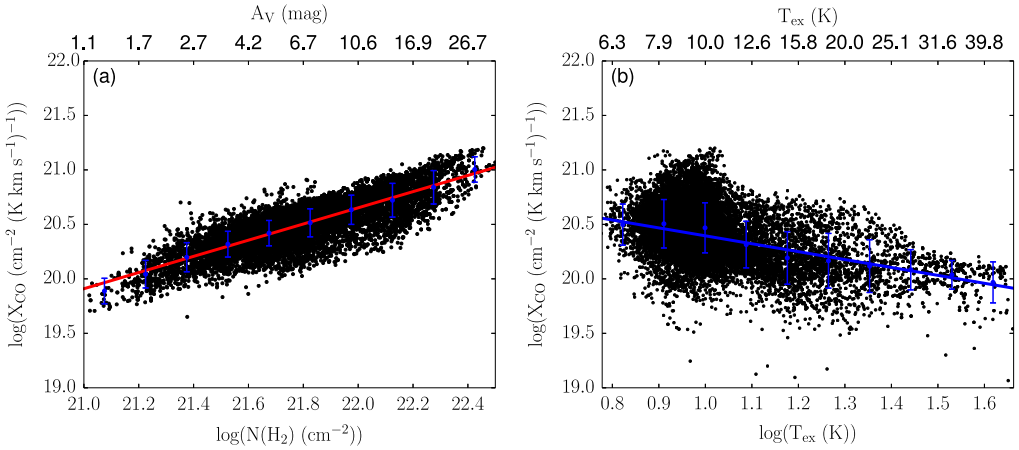

Figure 16. Relations between (a) X_{CO} and $N(H_2)$ in cold tiles (excluding tiles 11–14) and (b) X_{CO} and T_{ex} in the entire CMC. Red (a) and blue (b) lines represent least-squares fits to unbinned and binned (every 0.09 dex) data, respectively. The typical uncertainties in the *X*-factor are between 5% and 7%.

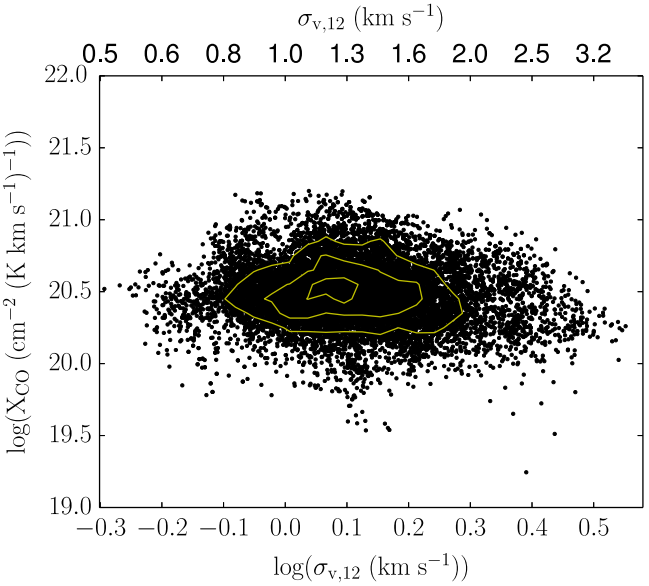

Figure 17. X_{CO}–$\sigma_{v,12}$ relation for cold tiles, excluding tiles 11–14. The yellow contours show the surface density of points. There appears to be no strong correlation between these two quantities.

OB stars or H II regions, Pineda et al. (2010) find $X_{CO} = 2.1 \times 10^{20}\,\mathrm{cm^{-2}}\left(\mathrm{K\ km\ s^{-1}}\right)^{-1}$ from CO observations of that cloud. A relatively high value ($2.54 \times 10^{20}\,\mathrm{cm^{-2}}\left(\mathrm{K\ km\ s^{-1}}\right)^{-1}$) for X_{CO} was also derived from *Planck* observations of high-latitude diffuse and presumably cold, CO gas (Planck Collaboration et al. 2011). We noted earlier that the global *X*-factor for the CMC was 25% higher than the Milky Way value, and this may be due to the relatively large tracts of cold regions included in the average for the CMC. Of course, variations in velocity dispersions between clouds could also contribute to the variation in their observed *X*-factors. However, we would expect similar velocity dispersions to characterize gravitationally bound or virialized clouds of similar mass and size. Moreover, since the average column densities of molecular clouds are also constant (e.g., Larson 1981; Lombardi et al. 2010), we would expect $\langle X_{CO}\rangle \sim \langle T\rangle^{-1}$ for such clouds. As recently pointed out by Narayanan & Hopkins (2013), Galactic GMCs are characterized by very similar physical properties resulting in *X*-factors that span a relatively narrow range of values. They suggest that this is a result of the competition between stellar feedback and gravity that is necessary to maintain the relative stability of these objects. Here we are suggesting that variation within that narrow range of observed X_{CO} may be due to variations in the relative fractions of hot gas in these clouds. This hot gas, of course, is a direct product of the amount of stellar feedback the clouds are experiencing. Resolved maps of the internal *X*-factor distribution in additional clouds would be useful to determine the relative contribution of temperature to the derived values of X_{CO} within GMCs in general and could directly test this idea.

Absent of such additional data, it is instructive to compare our observations to recent simulations of turbulent cloud evolution that resolve synthetic clouds and derive the internal spatial distribution of the *X*-factor (Shetty et al. 2011a, 2011b). These simulations are thus directly comparable to observations such as ours. The Shetty et al. simulations include chemical evolution and radiative transfer to enable predictions of CO line emission. However, the calculations do not include gas-dust chemical interactions and are thus not relevant to our earlier findings or discussion regarding [^{13}CO], [C^{18}O], and $W(^{13}\mathrm{CO})/W(\mathrm{C}^{18}\mathrm{O})$. But since ^{12}CO is so optically thick, we safely assume that effects of depletion/desorption are not important for our *X*-factor determinations, and thus comparisons with these models are appropriate. Because the Shetty et al. simulations do not incorporate stellar feedback, the most appropriate comparison will be with our data in the regions of the CMC away from the embedded cluster (all tiles excluding 11–14). The simulated cloud of Shetty et al. (2011b), whose physical conditions match most closely those of typical GMCs, is characterized by a global X_{CO} lower than we observe in the cold tiles of the CMC map (2.2 versus $3.4 \times 10^{20}\,\mathrm{cm^{-2}}\left(\mathrm{K\ km\ s^{-1}}\right)^{-1}$) but closer to the Milky Way value. On sub-cloud scales Shetty et al. (2011b) find a correlation between X_{CO} and A_V (see their Figure 4) similar to but somewhat weaker than what we observe in the CMC. The simulations also predict that there should be a correlation between the *X*-factor and the velocity dispersion in the cloud, with $X_{CO} \propto \sigma_{V12}^{-0.5}$. In Figure 17 we plot X_{CO} against the velocity dispersion, σ_{V12} in the cold cloud regions.[13] We find no correlation between these same quantities, contrary to the predictions of the simulation. Although the simulations of individual clouds do not include any systematic temperature gradients or increases due to stellar heating, simulations were performed to investigate how increasing the overall cloud temperature can affect X_{CO}. These simulations predict a trend of decreasing *X* with *T*, consistent with what we observe here. The simulations find $X_{CO} \propto T^{-0.5}$ for different temperature clouds, which is only somewhat weaker than what is observed here, i.e., $X_{CO} \propto T^{-0.7}$ within the CMC. Overall, we conclude that the agreement between these simulations and the CMC is mixed, and it is unclear whether any similarities between the simulations and the observations of the CMC are more than coincidental.

5. SUMMARY AND CONCLUSIONS

In this study we presented the results of extinction and molecular-line mapping toward the most active star-forming region within the nearby California GMC. The relationship between dust and gas properties in this active portion of the cloud was investigated with the following results.

1. The LTE molecular abundances of ^{13}CO and C^{18}O in the cloud exhibit significant spatial variations. These variations are correlated with the spatial variation in gas (and presumably dust) temperature in the cloud. These temperature variations are likely caused by the heating from the adjacent, partially embedded, LkHα 101 cluster. We argue that the spatial variations in the derived ^{13}CO and C^{18}O gas abundances are largely due to temperature-dependent gas depletion/desorption on/off dust grains.
2. The abundance ratio between ^{13}CO and C^{18}O increases in lower-extinction regions of the CMC, suggesting

[13] σ_{V12} is the second moment of the ^{12}CO(2–1) profile $\equiv \left(\frac{\int T_{mb}(v-\mathrm{M1})^2 dv}{\int T_{mb} dv}\right)^{\frac{1}{2}}$, where M1 is the first moment $\int v T_{mb} dv$. σ_{V12} equals the velocity dispersion if line profile is Gaussian.

selective photodissociation of $C^{18}O$ in those regions. This is likely caused by ambient UV radiation, which apparently penetrates relatively deeply (i.e., $A_V \lesssim 15$ mag) into the cloud, particularly near the embedded cluster. There is also evidence that the selective photodissociation of $C^{18}O$ can suppress its abundance even in warm regions heated by the embedded cluster where evaporation off grain surfaces would otherwise lead to an increase in the $C^{18}O$ abundance at these cloud depths.

3. Dramatic spatial variations are also observed in the relationship between the ^{12}CO integrated intensity, $W_{^{12}CO(2-1)}$, and A_V, particularly at the intermediate and high extinctions ($A_V \gtrsim 3$–5 mag) primarily probed in this study. However, unlike the case for its two rarer isotopologues, the variation in ^{12}CO integrated intensity appears to be a direct result of a spatial gradient of the excitation temperature (and gas kinetic temperature) with extinction and not the result of any detectable variation in the ^{12}CO abundance due to depletion/desorption effects.
4. We compute the X-factor ($= N(H_2)/W(CO)$) for each individual pixel in our map and average the results to obtain $\langle X_{CO}\rangle = 2.53 \times 10^{20}\,\mathrm{cm^{-2}}\left(\mathrm{K\,km\,s^{-1}}\right)^{-1}$, a value somewhat higher than the Milky Way average.
5. On the sub-parsec scales in the CMC there is no single empirical value of the ^{12}CO X-factor that can characterize the molecular gas in cold ($T_k \lesssim 15$ K) regions with $A_V \gtrsim 3$ mag. For those regions we find that $X_{CO} \propto A_V^{0.7}$ with $\langle X_{CO}\rangle = 3.4 \times 10^{20}\ \mathrm{cm^{-2}}\left(\mathrm{K\,km\,s^{-1}}\right)^{-1}$. We do, however, find a clear correlation between $W(^{12}CO)$ and A_V in regions containing relatively hot ($T_{ex} \gtrsim 25$ K) molecular gas at $A_V \gtrsim 3$ mag, suggesting that, unlike the cold gas, the warm material may be characterized by a single value of X_{CO}. However, in this warm gas we find a value for the X-factor, $X_{CO} = 1.5 \times 10^{20}$ $\mathrm{cm^{-2}}\left(\mathrm{K\,km\,s^{-1}}\right)^{-1}$, significantly lower than the averages for the cold gas, the overall CMC, and the Milky Way.
6. Overall we find an (inverse) correlation between X_{CO} and T_{ex} with $X_{CO} \propto T_{ex}^{-0.7}$. Such a correlation may potentially explain the observed variations in global X-factors between GMCs as being due in large part to variations in the relative amounts of warm gas heated by OB stars within the clouds.

We thank Kelsey Jorgenson for assistance with acquiring the CO observations and acknowledge useful discussions with Karin Öberg. Suggestions from an anonymous referee led to numerous improvements in the paper. Carlos Roman acknowledges support from CONACYT project CB2010-152160, Mexico. This research is based in part on observations collected at the Centro Astronómico Hispano Alemán (CAHA) at Calar Alto, operated jointly by the Max-Planck-Institut für Astronomie and the Instituto de Astrofísica de Andalucía (CSIC). The Heinrich Hertz Submillimeter Telescope is operated by the Arizona Radio Observatory, which is part of the Steward Observatory at the University of Arizona. This work was supported in part by National Science Foundation grant AST-1140030 to the University of Arizona.

REFERENCES

Ackermann, M., Ajello, M., Allafort, A., et al. 2012, ApJ, 756, 4
Alves, J., Lada, C. J., & Lada, E. A. 1999, ApJ, 515, 265
Alves, J. F., Lada, C. J., & Lada, E. A. 2001, Natur, 409, 159
Alves, J., Lada, C. J., Lada, E. A., Kenyon, S. J., & Phelps, R. 1998, ApJ, 506, 292
Bergin, E. A., Alves, J., Huard, T., & Lada, C. J. 2002, ApJL, 570, L101
Bergin, E. A., Ciardi, D. R., Lada, C. J., Alves, J., & Lada, E. A. 2001, ApJ, 557, 209
Bergin, E. A., Langer, W. D., & Goldsmith, P. F. 1995, ApJ, 441, 222
Bergin, E. A., & Tafalla, M. 2007, ARA&A, 45, 339
Bieging, J. H., Peters, W. L., & Kang, M. 2010, ApJS, 191, 232
Bohlin, R. C., Savage, B. D., & Drake, J. F. 1978, ApJ, 224, 132
Bolatto, A. D., Wolfire, M., & Leroy, A. K. 2013, ARA&A, 51, 207
Caselli, P., Walmsley, C. M., Tafalla, M., Dore, L., & Myers, P. C. 1999, ApJL, 523, L165
Dickman, R. L. 1978, ApJS, 37, 407
Digel, S. W., Aprile, E., Hunter, S. D., Mukherjee, R., & Xu, F. 1999, ApJ, 520, 196
Forbrich, J., Öberg, K., Lada, C. J., et al. 2014, A&A, 568, A27
Frerking, M. A., Langer, W. D., & Wilson, R. W. 1982, ApJ, 262, 590
Goldsmith, P. F., & Langer, W. D. 1978, ApJ, 222, 881
Goodman, A. A., Pineda, J. E., & Schnee, S. L. 2009, ApJ, 692, 91
Harvey, P. M., Fallscheer, C., Ginsburg, A., et al. 2013, ApJ, 764, 133
Kramer, C., Alves, J., Lada, C. J., et al. 1999, A&A, 342, 257
Lada, C. J., Lada, E. A., Clemens, D. P., & Bally, J. 1994, ApJ, 429, 694
Lada, C. J., Lombardi, M., & Alves, J. F. 2009, ApJ, 703, 52
Lada, C. J., Lombardi, M., & Alves, J. F. 2010, ApJ, 724, 687
Langer, W. D., & Penzias, A. A. 1993, ApJ, 408, 539
Larson, R. B. 1981, MNRAS, 194, 809
Lee, M.-Y., Stanimirović, S., Wolfire, M. G., et al. 2014, ApJ, 784, 80
Levine, J. 2006, PhD thesis, Univ. Florida
Li, D. L., Esimbek, J., Zhou, J. J., et al. 2014, A&A, 567, A10
Lombardi, M. 2009, A&A, 493, 735
Lombardi, M., & Alves, J. 2001, A&A, 377, 1023
Lombardi, M., Alves, J., & Lada, C. J. 2006, A&A, 454, 781
Lombardi, M., Alves, J., & Lada, C. J. 2010, A&A, 519, LL7
Narayanan, D., & Hopkins, P. F. 2013, MNRAS, 433, 1223
Pineda, J. E., Caselli, P., & Goodman, A. A. 2008, ApJ, 679, 481
Pineda, J. L., Goldsmith, P. F., Chapman, N., et al. 2010, ApJ, 721, 686
Planck Collaboration, Ade, P. A. R., Aghanim, N., et al. 2011, A&A, 536, AA19
Rachford, B. L., Snow, T. P., Destree, J. D., et al. 2009, ApJS, 180, 125
Ripple, F., Heyer, M. H., Gutermuth, R., Snell, R. L., & Brunt, C. M. 2013, MNRAS, 431, 1296
Röllig, M., & Ossenkopf, V. 2013, A&A, 550, A56
Román-Zúñiga, C. G. 2006, PhD thesis, Univ. Florida
Román-Zúñiga, C. G., Alves, J. F., Lada, C. J., & Lombardi, M. 2010, ApJ, 725, 2232
Sandstrom, K. M., Leroy, A. K., Walter, F., et al. 2013, ApJ, 777, 5
Sault, R. J., Teuben, P. J., & Wright, M. C. H. 1995, adass, 77, 433
Shetty, R., Glover, S. C., Dullemond, C. P., et al. 2011a, MNRAS, 415, 3253
Shetty, R., Glover, S. C., Dullemond, C. P., & Klessen, R. S. 2011b, MNRAS, 412, 1686
Shimajiri, Y., Kitamura, Y., Saito, M., et al. 2014, A&A, 564, A68
Solomon, P. M., Rivolo, A. R., Barrett, J., & Yahil, A. 1987, ApJ, 319, 730
Taylor, M. B. 2005, adass, 347, 29
van der Tak, F. F. S., Black, J. H., Schöier, F. L., Jansen, D. J., & van Dishoeck, E. F. 2007, A&A, 468, 627
van Dishoeck, E. F., & Black, J. H. 1988, ApJ, 334, 771
van Dishoeck, E. F., Blake, G. A., Draine, B. T., & Lunine, J. I. 1993, Protostars and Planets III, ed. E. H. Levy, & J. I. Lunine (Tucson, AZ: Univ. Arizona Press), 163
Visser, R., van Dishoeck, E. F., & Black, J. H. 2009, A&A, 503, 323